




Article

Prediction of Angular Distortion in Gas Metal Arc Welding of Structural Steel Plates Using Artificial Neural Networks

Kuluthupalayam Maruthavanan Eazhil ¹, Ranganathan Sudhakaran ^{1,*}, Elumalai Perumal Venkatesan ² , Abdul Aabid ³  and Muneer Baig ³ 

¹ Department of Mechanical Engineering, SNS College of Engineering Coimbatore, Tamilnadu 641107, India

² Department of Mechanical Engineering, Aditya Engineering College, Surampalem 533437, India

³ Department of Engineering Management, College of Engineering, Prince Sultan University, Riyadh 11586, Saudi Arabia

* Correspondence: absudha@yahoo.com

Abstract: The manufacturing of structures ranging from bridges and machinery to all types of seaborne vehicles to nuclear reactors and space rockets has made considerable use of arc welding technologies. This is as a result of benefits including increased joint efficiency, air and water tightness, no thickness restriction (0.6 to 25 mm), decreased fabrication time and cost, etc. when compared to alternative fabrication methods. Gas metal arc welding (GMAW) is a frequently used welding technology in industries due to its inherent benefits, including deeper penetration, a smooth bead, etc. Local heating and cooling that takes place during the multi-pass welding process causes complicated stresses to develop at the weld zone, which ultimately causes angular distortion in the weldment. Angular distortion is a major flaw that affects the weld's properties as well as the cracking and misalignment of the welded joints. The issue of angular distortion can be successfully solved by predicting it in relation to certain GMAW process variables. A neural network model was created in this research to predict angular distortion. A fractional factorial approach with 125 runs was used to conduct the exploratory experiments. A neural network model with feed forward and backward propagation was developed using the experimental data. To train the neural network model, the Levenberg–Marquardt method was utilised. The results indicate that the model based on network 4-9-3 is more effective in forecasting angular distortion with time gaps between two, three, and four passes than the other three networks (4-2-3, 4-4-3, 797 and 4-8-3). Prediction accuracy is more than 95 percent. The neural network model developed in this study can be used to manage the welding cycle in structural steel weld plates to achieve the best possible weld quality with the least amount of angular distortion.

Keywords: structural steel; gas metal arc welding; angular distortion; artificial neural networks



Citation: Eazhil, K.M.; Sudhakaran, R.; Venkatesan, E.P.; Aabid, A.; Baig, M. Prediction of Angular Distortion in Gas Metal Arc Welding of Structural Steel Plates Using Artificial Neural Networks. *Metals* **2023**, *13*, 436. <https://doi.org/10.3390/met13020436>

Academic Editors: João Pedro Oliveira and Marcello Cabibbo

Received: 31 December 2022

Revised: 6 February 2023

Accepted: 7 February 2023

Published: 20 February 2023



Copyright: © 2023 by the authors. Licensee MDPI, Basel, Switzerland. This article is an open access article distributed under the terms and conditions of the Creative Commons Attribution (CC BY) license (<https://creativecommons.org/licenses/by/4.0/>).

1. Introduction

Welding methods have been used in the production of a wide range of objects, such as bridges, equipment, nuclear reactors, and the space shuttle. This is due to its excellent joint efficiency, ability to weld complex structural geometries, and reduced fabrication costs as compared to alternative joining processes. Jiajia Shen et al. [1,2] GMAW welding is mostly applied for welding of automobile chassis parts where it is necessary to secure the strength and rigidity of the joint. In the construction industry, it has been used for welding of components in bridges dam and manufacturing plants. It is also used for structurally sound metal frame works. Robotic assembly lines typically use GMAW for production techniques that are time-effective. Jiajia Shen et al. [3] Structural steel is a type of mild steel that has a low carbon content of 0.25 to 0.35 percent and a manganese content of 1.4 percent. Si, S, and P are equally important for weldability, even though carbon is the

alloying ingredient that is most important. Their importance can be assessed by converting them to carbon equivalents. Due to the characteristics of fusion based welding, especially due to the non-equilibrium solidification conditions, as well as the existence of fast heating and cooling cycle and high peak temperature results in problem such as fracture arrest, material sensitivity, residual stress and distortion. The source of all of these problems is the welding heat cycle, which occurs in the weld metal and base metal components of the weldment. In large steel fabrications, welding distortion leads to dimensional inaccuracies and misalignments of structural members. Rework or corrective actions are necessary when tolerance thresholds are crossed. Production costs increase as a result, and delivery times grow longer. In fabricated constructions, distortion during welding leads to three primary dimensional changes: Two types of shrinkage occur: (a) longitudinal shrinkage parallel to the weld line; and (b) transverse shrinkage perpendicular to the weld line. (c) Rotation or deformation around the weld line Since angular distortion has a more significant impact than the other two fundamental distortions, it is given priority. Before welding, the plates can be pre-bent in plastic or pre-strained in elastic to help minimise normal distortion. For this to occur, precise angular distortion prediction under a particular set of operational circumstances is necessary. Angular distortion is significantly influenced by the welding process parameters. Since predicting angular distortion and figuring out the ideal welding process parameters both require expensive and time-consuming trials, it is challenging to predict angular distortion with precision for a particular set of operating parameters. This is due to the complicated and nonlinear nature of the welding process. It is necessary to create a suitable model, optimise the process parameters, and anticipate and reduce angular distortion. More effective techniques, such as artificial neural networks, are needed to anticipate angular distortion and determine the ideal welding process parameters.

Statistical methods help to see and understand any patterns within the data. It is challenging to determine why one system performs better than another without statistical models. It provides intuitive visualisation that makes it easier to see how different factors relate to one another and make predictions. The statistical method does not focus on qualitative aspect and the results are true only on average whereas FEM requires large amount of data as input for the mesh. The output result will vary considerably. The neural network mode offers numerous advantages such as the ability to implicitly detect complex nonlinear relationships between dependent and independent variable. Koichi Masubuchi [4] studied the angular distortion that occurs at butt, lap, T, and corner joints when single-sided or asymmetrical double-sided welding is used. They found that the degree of angular distortion depends on the width and depth of the fusion zone in relation to the plate thickness, joint type, weld pass sequence, and thermo-mechanical material properties. Choobi et al. [5] used artificial neural networks to anticipate angular distortion when welding 304-grade stainless steel plates in a single pass. They run a series of finite element simulations for different plate sizes to provide the data for the neural network model. Paulo Cezar et al. [6] discovered that the neural network model they had created was able to predict angular distortions during the welding of single-pass plates that were butt welded with accuracy. Mohd Hafiza Abdul Kadir et al. [7] examined the behaviour of angular distortion in ASTM A36 structural steel plates welded using the GMAW process. They varied the heat inputs between 0.6 and 2.5 kJ/min and built three equations in order to predict angular distortion. They came to the conclusion that the model that was built with the least amount of heat input could correctly forecast angular distortion. Woo-Jae Seong [8] proposed a method for predicting transverse angular distortion in multi-layer butt welding. He developed a algorithm to save saves computational time using databases and geometry based on a numerical approach.

Navid Ansari pour et al.'s [9] research on the submerged arc welding method concentrated on minimising distortion and residual processing. By running tests with varying cooling times and welding rates between the first and second passes, they were able to collect training data. An artificial neural network model was created based on the training data. The optimised, trained neural network was then input into single- and multi-objective

genetic algorithms and single- and multi-objective harmony search techniques. Using the findings as a guide, single- and multi-objective optimization techniques are utilised to lessen residual stress and distortion.

An approach based on inherent strain was used by Vishvesha et al. [10] to analyse the distortion in the GBC's (Guide Blade Carrier) outer ring. They came to the conclusion from their investigation that, using the above-described method, they could predict 3-D distortion patterns with accuracy. They also found a strong correlation between projected and observed values. A technique for computing deformation was developed by Wu et al. [11] to more precisely estimate welding distortion. The welding-induced bending deformation is calculated using this algorithm as a function of the bending angle. The authors concluded that the algorithm was able to accurately estimate angular distortion in terms of bending angle. Using gas tungsten arc welding, Zubairuddin et al. [12] investigated the distortion of 3 mm-thick modified 9Cr-1Mo steel plates. The distortion was measured using a vertical electronic height gauge. They created a 3D mesh model using the SYSWELD programme to simulate deformation. They utilised both big and small distortion theories for the finite element analysis of the weld joint. As a result of their analysis, they came to the conclusion that the huge distortion theory yields precise experimental and numerical results.

Venkatesan et al. [13] investigated the 409 M ferritic stainless steels bending distortion. In order to identify the bowing distortion, the investigators used a profile tracer and a flux-cored arc welding technique. By developing a regression equation linking the welding process parameters and bending distortion, the impacts of process factors such as welding current, travel speed, voltage, and CO₂ shielding gas flow rate were examined. The regression equation was used to find the ideal values for the process parameters to achieve the least distortion. Suman et al. [14] developed an enhanced equivalent load-based method to predict welding distortions in large weld structures. When analysing a large weld structure, the transient character of plastic strain distribution was taken into consideration. The proposed method was validated by comparing the outcomes to the experimental data. Comparing the two showed that they are perfectly compatible. The procedure was validated by measuring welding distortions for various welding joints in order to make sure it was effective. Ronget et al. [15] developed a hybrid model using non-linear yield stress curves and multi-constraint equations in thermoplastic analysis for predicting welding deformities in large-scale constructions. The dependability of the integration model is supported by published experimental results of GMAW-welded T-joint structural steel S355JR. The results show that the suggested integration model can reduce computation time by 30.14 percent. The hybrid model can therefore be used to precisely predict welding distortions in massive structures.

Wang et al. [16] investigated the distribution of deformation and residual stress in lifting lugs, a frequently employed welded construction in the shipbuilding industry. They recommended using a heat compensation strategy to boost lifting lug output. Based on their numerical and experimental results, they came to the conclusion that the coupled finite element model may be used successfully to address the challenges of industrial production and that the proposed thermal compensation method may boost productivity.

For CO₂ laser-MIG hybrid welding, Chaki et al. [17] developed an artificial neural network (ANN) model to predict the relationship between laser power, welding speed, wire feed rate, and tensile strength. They used a full-factorial experimental design to gather data. A back-propagation algorithm was applied to radial function networks as a training method. To find the model with the best predictive power, the authors have developed 65 different architectures and tested them using 6 different training methods. They discovered that the network 3-11-1 had a mean square error of 3.24×10^{-4} and correctly predicted the outcome.

Using the Gas Tungsten Arc Welding (GTAW) method, Sudhakaran et al. [18] carried out experiments on stainless steel plates of grade 202 in order to forecast the angular distortion by creating an ANN model. A central composite five-factor level rotatable design is used for the tests and data collection. Using the Levenberg–Marquette method, a feed-forward backward propagation neural network model was trained on the experimental data. They came to the

conclusion that the ANN model could predict angular distortion accurately. Pazooki et al. [19] studied the distortion that happens in GMAW of $500 \times 250 \times 6$ mm 3AH36 plates using both experimental and numerical methods. They created a 3D finite element model to better comprehend the distortion mechanism. The model was validated using temperature, distortion, residual stress, and microstructure investigations. It is found that the numerical analytical results and the experimental data are extremely close.

Barclay et al. [20] employed ANN to estimate the refinement of weld distortion using a travelling induction coil. The weld specimen was heated using a voyage, which is an induction coil. To predict weld-induced distortion and its rectification using a travelling induction coil, an ANN model was built based on experimental data. The results show that distortion in DH36 steel plates with a thickness of 6 mm may be fully eliminated and that distortion in plates with a thickness of 8 mm and 10 mm can be greatly reduced. Liang Tian et al. [21] used the bead-on-plate method to anticipate angular distortion and transverse shrinkage and created a back-propagation neural network model for gas tungsten arc welding for S304L stainless steel plates. To mimic the welding process, they used a finite element method. The neural network model was also evaluated using experiment data. The experiment's input parameters included welding voltage, welding current and welding speed. The output parameters were transverse shrinkage and angle distortion. They deduced from the findings that the neural network model could predict angular distortion properly. Using a numerical and artificial neural network model, Cristian Rubio-Ramirez et al. [22] predicted angular distortion in the GMAW process of thin-sheet Hardox 450[®] steel. Comsol Multiphysics' thermo-elastic-plastic model was used to create the 3D finite element model. The finite element model was validated through a number of trials. They developed a model that included the effects of heat input, filler metal dilution percentage, and angular distortion. The neural network model received the finite element model's outputs as input data. The deformation and residual stresses in 20-mm-thick austenitic stainless steel plates welded using the GTAW technique was examined by Sayantan Das Banik et al. [23]. Heat input, welding speed, and restrictions are the variables taken into account during the inquiry. Distortion and residual strains were the outputs that were measured. They performed the heat study and used FEM to model the weld joint. They deduced from the analysis that there was good agreement between the experimental and numerical results. The effects of welding parameters and welding method on residual stress and distortion in Al6061-T6 aluminium alloy for a T-shaped welded joint using GMAW technology were examined by Amirreza Khoshroyan et al. [24]. They created a three-dimensional thermo-mechanical coupled finite element model with the use of Ansys software to analyse distortion as a function of welding current, welding speed, and welding sequence. They discovered that while welding speed causes angular distortion to decrease, welding current induces plate and stiffener deformation. The alteration in welding procedure caused the deformation to spread throughout the entire plate. Garca-Garca et al. [25] developed a finite element model to simulate welding residual stresses and deformation in Ti-containing TWIP steel. The welding heat cycle of TWIP-Ti steel was investigated using the thermo-mechanical model. The residual stress crucial zone was defined using maximum tensile residual stress and hardness, two properties found in the fusion zone and the heat-impacted zone. To validate the results, X-ray diffraction was performed at the welds' crucial areas. As a result of their research, they were able to quantify improved weldability for TWIP-Ti steel throughout the GTAW process.

Venkat Kumar et al. [26] used finite element analysis to analyse the effects of heat on temperature, distortion, and residual stress in butt-welded plates. They investigated the effects of five different heat inputs on the weld bead shape, residual stress, and distortion of 304 stainless steel butt welded plates using 3D finite element analysis. Based on the results, they came to the conclusion that heat significantly affects welding distortion and residual strains. Vasantharja et al. [27] examined the deformation and residual stresses in 316LN stainless steel weld joints produced by both TIG and A-TIG methods for various joint configurations. After radio graphing the weld connections, the microstructure was

characterised using an optical microscope. The distortion was calculated using a height gauge. Their investigation led them to the conclusion that double-sided A-TIG welding produced the least distortion in weld connections. Remaining stresses and distortion in the gas metal arc welding of two thin, different aluminium alloy plates, AA5052 and AA6061, were examined by Tapas Bajpei et al. [28]. The distortion of the weld samples was assessed using coordinate measurement equipment. The results were validated using a three-dimensional thermo-mechanical finite element model made with the ANSYS programme. They came to the conclusion that the numerical and experimental data were in good agreement and that the AA6061 plates shrank considerably less than the AA5052 plates based on their comparison. Laksha et al. [29] explored angular distortion in the MIG welding process by creating a mathematical model. The mathematical model was developed by linking welding process variables to angular distortion. The tests were created using a central composite rotatable design, and the model's applicability was then examined. The results were graphically examined using the Response Surface Methodology. The analysis led them to the conclusion that the mathematical model could correctly forecast angular distortion.

In order to predict angular distortion in structural steel plates that had been connected by gas metal arc welding, Lohate and damale et al. [30] focused on studying the effect of process variable such as arc voltage, travel speed, welding current, wire feed rate, gas flow rate on angular distortion. Fuzzy logic has been employed for prediction of angular distortion. The effects of process parameters were represented graphically and compared with the experimental results. The outcome of the research was the results obtained by Fuzzy logic tools shows agreement with the experimental results. Baskoro et al. [31] examined how GMAW variables impacted the deformation of A36 mild steel. To determine the welding process settings that would cause the least amount of distortion, they used the Taguchi technique. They used welding current and speed as the input and angular distortion as the response. The trial runs are carried out using a L9 orthogonal array. The minimal criteria were defined using the S/N ratio and the quality character "smaller is better." The findings demonstrate that a welding current of 170 A and a welding speed of 4.0 mm/s can create the least amount of distortion, with welding speed having a bigger impact on angular distortion. DeqiaoXie et al. [32] used an asymmetric cross-sectional form on the thickness side to explore the cause of angular distortion in fusion welding. They developed a mathematical model that connected the melting-solidification process to angular distortion. The experiments were carried out using laser welding on 316L stainless steel, and the results were compared with the expected values. Based on the results, they came to the conclusion that an asymmetric cross-sectional profile significantly leads to angular distortion. Yu R et al. [33] researched the weld reinforcement prediction in the GMA additive manufacturing process using the visual-sensing system for molten pool and created a laser locating method to match every frame of the molten pool image with the actual weld site. They created the prediction model for weld reinforcement in the GMA additive manufacturing process by extracting the shape and location properties of the molten pool as visual features using a back-propagation (BP) neural network. They concluded from their experimental investigation that the model could correctly forecast welding reinforcement.

The primary cause of angular distortion was plastic deformation of the work piece in an angular direction caused by uneven contraction along the thickness. Factors including the relative depth of penetration, the relative bead width and shape, and the mechanical and thermal properties of the base and filler material all have an impact on the creation of angular deformation. Angular distortion is controlled by welding process settings that regulate bead geometry, welding speed, wire feed rate, time between passes, nozzle to plate angle, number of passes, voltage, and current—all critical welding parameters that determine angular distortion. The most common method for predicting angular distortion was simulation using finite element analysis, whereas ANN can be used for more precise predictions. For performing trials, the majority of studies employed either Taguchi Design or Central Composite Rotatable Design; however, additional test data is required for

constructing an ANN model. As a result, the experiments in this study were carried out using fractional factorial with 125 experimental runs. A neural network structure with four input neurons, three output neurons, and several nodes in the hidden layer was constructed using the experimental data. The networks 4-2-3, 4-4-3, 4-8-3, and 4-9-3 are engaged. The input parameters for the networks were time between passes (t), angle of electrode with work piece (θ), wire feed rate (F), welding speed (S), and number of passes (N). At the end of the second, third, and fourth passes (two, three, and four, respectively) of the welding process, the output parameter angular distortion (α) was measured. The network was developed using the Levenberg–Marquardt method. In comparison to the other networks, the ANN model based on 4-9-3 were better at predicting angular distortion at the conclusion of the second, third, and fourth passes.

2. Experimental Process

Data must be produced through experiments that are representative of actual fabrication circumstances in order to study how process control parameters affect angular distortion. In order to effectively develop a mathematical/neural network model, the experiments should be conducted in a systematic approach this will enable to study the relationship between multiple input variables and key output variables. Finally, we would be able to get the desired results of minimizing angular distortion.

To conduct experiments, a well-prepared and designed experimental plan and programme are required. The studies were carried out using a design matrix based on fractional factorials and 125 experimental runs. The base metal for the current investigations was 300 mm \times 150 mm \times 25 mm of IS: 2062 (Grade A) structural steel made by Steel Authority of India Limited (SAIL). The filler material used to weld the specimen is ER 70S—6 solid wire with a diameter of 1.2 mm. Table 1 shows the mild steel's chemical composition and key mechanical properties. The cross section of the specimen with edge preparation is shown in Figure 1. Parts 1–6 of EN 10025 are a set of European standards that define the technical delivery conditions for hot-rolled structural steel products. The current version is EN 10025:2019.

Table 1. Chemical composition of structural steel IS: 2062 Grade A.

C% (Max)	Mn% (Max)	S% (Max)	P% (Max)	Si% (Max)	CE% (Max)
0.23	1.50	0.050	0.050	0.40	0.42

Minimum yield strength = 240 MPa. Minimum ultimate tensile strength = 410 MPa. % of elongation = 23.

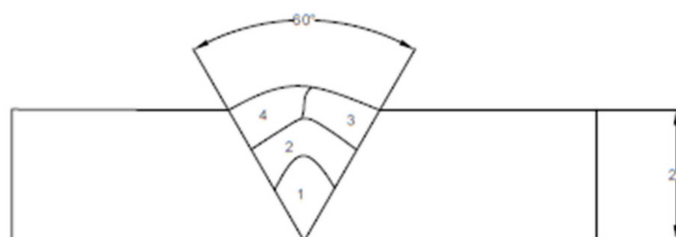


Figure 1. Cross section of the specimen.

A semi-automatic, thyristor-controlled metal-inert gas welding machine from M/s Icon Welding Equipment was used for all of the studies (Model IWE-MG-TC-400, 2019). The wire feed rate can be fine-tuned, and metres to display arc voltage and welding current are included on the control panel. The automatic MIG welding technique used a constant-potential (flat-characteristic) transformer and rectifier power supply. It had a supply voltage of 415 VAC at 50 or 60 Hz and could deliver currents ranging from 50 to 400 amps. The welding sample was moved in opposition to a fixed welding torch with the aid of a servo-motor-controlled linear manipulator. This linear manipulator can move the base plate in the X and Y directions at a predetermined welding speed, and to secure

the welding specimen, the base plate has a T-slot. The layout of the gas metal arc welding process is shown in Figure 2 and the experimental shown in Figure 3.

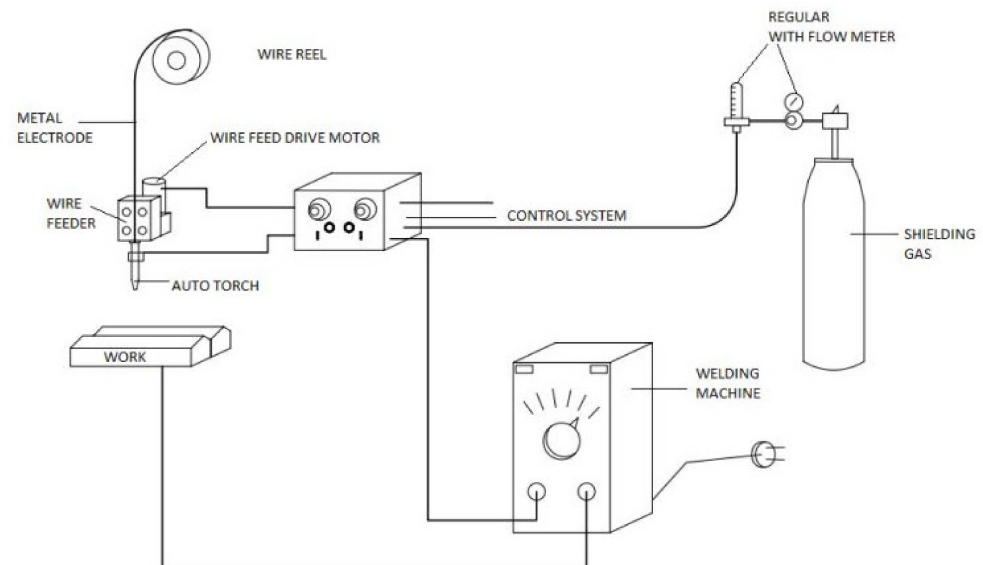


Figure 2. Layout of Gas Metal Arc Welding Machine.

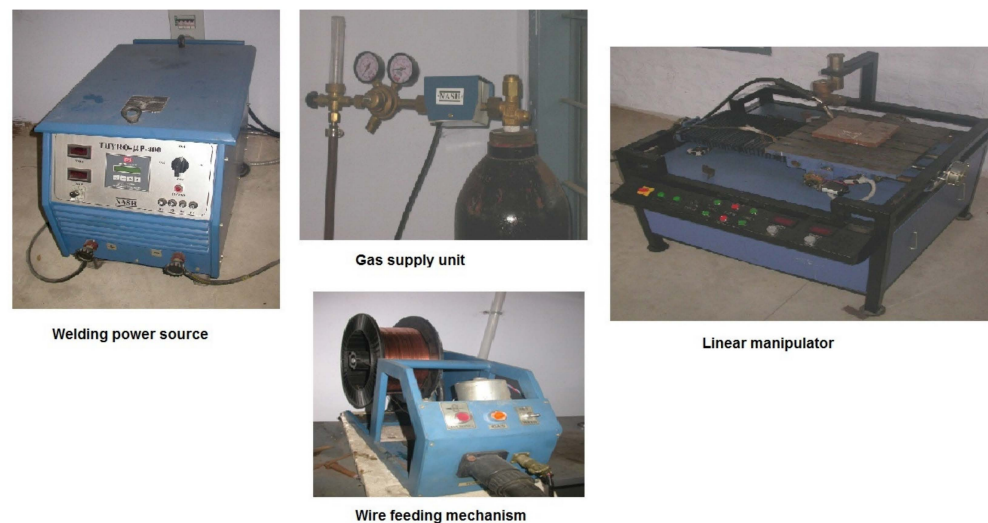


Figure 3. Experimental Setup.

3. Plan of Investigation

3.1. Choosing the Appropriate Design

The factorial design is the experimental design that will be used in this study. This is a common statistical method for conducting an experiment in the most efficient manner [34,35] and investigating the effects of variables on the response or output parameter. The most significant benefit of this design is that it allows for the simultaneous examination of a large number of factors, allowing for a better understanding of the combined impact of the parameters on the response. The experimental approach is to choose a predetermined number of levels for each parameter or factor before conducting trials with every possible combination of the parameters or factors. A fractional factorial with 125 experimental trial runs was selected as the study's design matrix [36–38].

3.2. Identification of the Process Variables

The best welding circumstances can be achieved by carefully choosing the independently controllable process variables or factors that affect weld quality. Among the several independently controllable process parameters affecting angular distortion, the angle of the electrode to the work piece (q), time gap between passes (t), wire feed rate (F), and welding speed (S) were selected as factors to carry out the experimental work and build mathematical models. Because welding current is dependent on the wire feed rate, it cannot be regulated directly. In place of welding current, wire feed rate was used as a factor. In MIG welding, open circuit voltage was used instead of arc voltage [39–42].

3.3. Determining the Limits of the Process Variables

All of the selected process variables' working ranges had to be established in order to fix their levels and create the design matrix. This was accomplished by conducting experimental runs in which one of the process variables was changed while the others remained constant. To determine the operating range of the process parameters, a large number of trial runs were carried out, and the weld bead was assessed for smoothness and any obvious flaws such as surface porosity, undercut, and so on. The following relationship was used to obtain the coded values for intermediate values: A factor's upper and lower bounds were both coded as +2 and −2, respectively.

$$X_i = \frac{2(2X - (X_{\max} + X_{\min}))}{(X_{\max} - X_{\min})} \quad (1)$$

where,

X_i —The required coded value of a variable X ,

X —Is any value of the variable from X_{\min} to X_{\max}

X_{\min} —Is the lower limit of the variable.

X_{\max} —Is the upper limit of the variable.

Table 2 shows the finalised levels of the selected process parameters in both GMAW trials, together with their units and notations.

Table 2. Welding process parameters and their levels.

Process Parameters	Units	Notation	Limits				
			−2	−1	0	+1	+2
Angle of electrode to work piece	Deg	θ	70	80	90	100	110
Time gap between passes	minutes	T	5	10	15	20	25
Wire feed rate	m/min	F	5	5.25	5.5	5.75	6
Welding speed	cm/min	S	8.4	9	9.6	10.2	10.8

3.4. Development of Design Matrix

The studies in factorial design try to investigate all conceivable combinations of parameter levels, and these combinations are recorded as a table, where the rows correspond to different trials and the columns to parameter levels, and they combine to produce a design matrix [43–46]. A total of 125 trial runs make up the design matrix. The design matrix is used to lay out the variables of the welding process. The design matrix allows for a systematic approach to conducting random experiments while also preventing systematic errors from entering the system [47].

3.5. Measurement of Angular Distortion

Using a laser cutter, structural steel plates (IS: 2062) of the required number of samples of 300 mm × 150 mm each were cut. A milling machine was used to prepare the edges for

the oxy-acetylene gas cutting machine by cutting a single “V” groove with a 30° included angle. Cutting fluids were used to reduce residual stresses created during machining, and the depth of cut was kept as low as feasible during groove preparation. This experiment looked at four welding process variables: angle of the electrode to the work piece (q), time gap between passes (t), wire feed rate (F), and welding speed (S). 125 experiments were conducted as per the design matrix. The welding sequence is shown in Figure 1, and the number of iterations was set to four. The angle of the electrode with the work piece is one of the process variables in this experiment (θ) [48–52]. It was also planned to conduct an analysis of angular distortion progress by measuring angular distortion at the end of the second, third, and fourth passes of welding (passes two, three, and four, respectively). The values of angular distortion corresponding to the time gap between the passes are represented as α_2 , α_3 and α_4 respectively [53–57]. In this study, the angular distortion at the end of the first pass is eliminated because the process variable time gap between passes (t) refers to the time between the end of the previous pass and the start of the current pass. The angular distortion won't be affected by the time interval between passes for the first pass because the first pass has no preceding pass. The response angular distortion (α) was measured using the following method: With the use of a vernier height gauge, the angular distortion (α) was measured using the sine bar concept. The ASTM A1030/A1030M-05 standard was used as the reference for angular distortion measurement. These established models are highly helpful in quantifying angular distortion in the negative direction, ensuring that the component will not have angular distortion after welding [58–62]. They can also be used to choose the best process parameters to reduce distortion in welded structures. Figure 4 illustrates the measurement principle for angular distortion. Figure 5 shows a welded specimen with varying degrees of deformation. In Table 3, the measured values of α are listed.

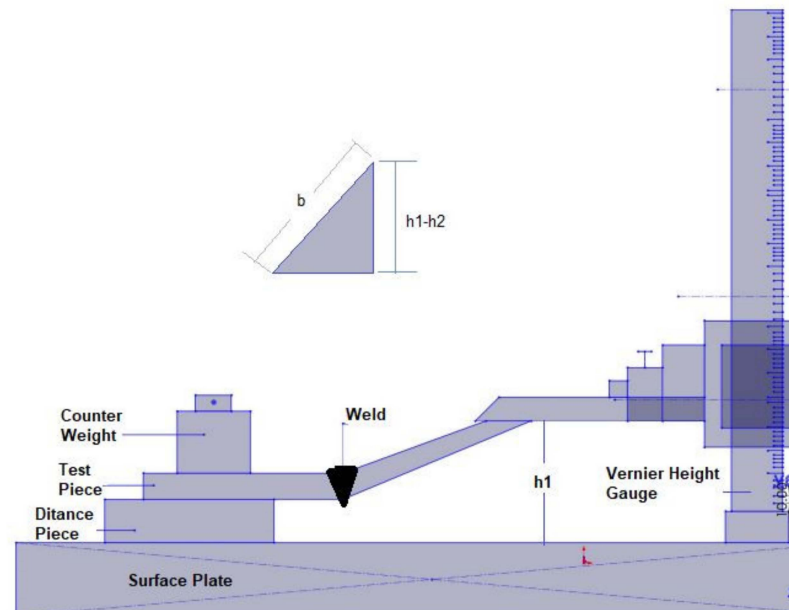


Figure 4. SINE BAR arrangement for measuring angular distortion.

$$\alpha = \sin^{-1} \left[\frac{h_1 - h_2}{b} \right] \quad (2)$$



Figure 5. Photograph showing angular distortion.

Table 3. Design matrix and measured value of angular distortion.

S. No.	θ	T	F	S	$\alpha 2$ Degrees	$\alpha 3$ Degrees	$\alpha 4$ Degrees
1	0	0	0	0	1.38	2.32	3.15
2	0	0	−1	2	1.88	2.44	2.81
3	0	0	0	1	1.38	2.22	2.96
4	0	0	1	0	1.34	2.3	3.03
5	0	0	2	−1	1.76	2.68	3.02
6	0	−1	0	2	1.56	2.02	2.57
7	0	−1	−1	1	2.32	3	3.62
8	0	−1	0	0	1.56	2.24	3.05
9	0	−1	1	−1	1.26	1.78	2.4
10	0	−1	2	0	1.42	2.2	2.71
11	0	0	0	1	1.38	2.22	2.96
12	0	0	−1	0	1.88	2.84	3.57
13	0	0	0	−1	1.38	2.22	2.96
14	0	0	1	0	1.34	2.3	3.03
15	0	0	2	2	1.76	2.38	2.45
16	0	1	0	0	1.2	2.24	3.05
17	0	1	−1	−1	1.44	2.5	3.22
18	0	1	0	0	1.2	2.24	3.05
19	0	1	1	2	1.42	1.89	2.09
20	0	1	2	1	2.1	3.01	3.18
21	0	2	0	−1	1.02	2.08	2.84
22	0	2	−1	0	1	2.02	2.77
23	0	2	0	2	1.02	1.24	1.43
24	0	2	1	1	1.5	2.2	2.56
25	0	2	2	0	2.44	3.46	3.61
26	−1	0	0	2	1.66	1.92	2.42
27	−1	0	−1	1	1.82	2.44	3.09
28	−1	0	0	0	1.4	2.1	2.94
29	−1	0	1	−1	1.44	2.06	2.71
30	−1	0	2	0	2.2	2.94	3.4
31	−1	−1	0	1	1.36	1.78	2.59
32	−1	−1	−1	0	1.78	2.26	2.94
33	−1	−1	0	−1	1.1	1.38	2.07
34	−1	−1	1	0	1.14	1.6	2.4
35	−1	−1	2	2	1.77	2.02	2.34
36	−1	0	0	0	1.4	2.1	2.94
37	−1	0	−1	−1	1.56	2.22	2.85
38	−1	0	0	0	1.4	2.1	2.94
39	−1	0	1	2	1.83	2.09	2.5
40	−1	0	2	1	2.33	2.95	3.33

Table 3. Cont.

S. No.	θ	T	F	S	α 2 Degrees	α 3 Degrees	α 4 Degrees
41	−1	1	0	−1	1.44	2.24	2.99
42	−1	1	−1	0	1.6	2.44	3.18
43	−1	1	0	2	1.83	2	2.36
44	−1	1	1	1	2.13	2.7	3.23
45	−1	1	2	0	2.89	3.7	4.02
46	−1	2	0	0	1.74	2.46	3.18
47	−1	2	−1	2	1.77	1.75	1.92
48	−1	2	0	1	1.87	2.29	2.83
49	−1	2	1	0	2.43	3.13	3.66
50	−1	2	2	−1	3.45	4.27	4.41
51	0	0	0	1	1.38	2.22	2.96
52	0	0	−1	0	1.88	2.84	3.57
53	0	0	0	−1	1.38	2.22	2.96
54	0	0	1	0	1.34	2.3	3.03
55	0	0	2	2	1.76	2.38	2.45
56	0	−1	0	0	1.56	2.24	3.05
57	0	−1	−1	−1	2.32	2.82	3.34
58	0	−1	0	0	1.56	2.24	3.05
59	0	−1	1	2	1.26	1.75	2.25
60	0	−1	2	1	1.42	2.19	2.66
61	0	0	0	−1	1.38	2.22	2.96
62	0	0	−1	0	1.88	2.84	3.57
63	0	0	0	2	1.38	1.92	2.39
64	0	0	1	1	1.34	2.2	2.84
65	0	0	2	0	1.76	2.78	3.21
66	0	1	0	0	1.2	2.24	3.05
67	0	1	−1	2	1.44	1.93	2.23
68	0	1	0	1	1.2	2.05	2.72
69	0	1	1	0	1.42	2.47	3.13
70	0	1	2	−1	2.1	3.19	3.46
71	0	2	0	2	1.02	1.24	1.43
72	0	2	−1	1	1	1.74	2.3
73	0	2	0	0	1.02	2	2.75
74	0	2	1	−1	1.5	2.56	3.12
75	0	2	2	0	2.44	3.46	3.61
76	1	0	0	0	1.58	2.54	3.36
77	1	0	−1	−1	2.42	3.26	3.91
78	1	0	0	0	1.58	2.54	3.36
79	1	0	1	2	1.07	1.71	2.04
80	1	0	2	1	1.41	2.41	2.71
81	1	−1	0	−1	2.24	2.72	3.37
82	1	−1	−1	0	3.08	3.76	4.4
83	1	−1	0	2	1.85	2.36	2.86
84	1	−1	1	1	1.47	2.22	2.89
85	1	−1	2	0	1.55	2.38	2.84
86	1	0	0	0	1.58	2.54	3.36
87	1	0	−1	2	2.03	2.63	2.98
88	1	0	0	1	1.45	2.33	3.05
89	1	0	1	0	1.33	2.33	3.04
90	1	0	2	−1	1.67	2.63	2.95
91	1	1	0	2	0.79	1.32	1.66
92	1	1	−1	1	1.37	2.28	2.91
93	1	1	0	0	1.05	2.12	2.94
94	1	1	1	−1	1.19	2.26	2.89
95	1	1	2	0	1.53	2.7	3

Table 3. Cont.

S. No.	θ	T	F	S	α 2 Degrees	α 3 Degrees	α 4 Degrees
96	1	2	0	1	0.39	1.15	1.73
97	1	2	−1	0	0.71	1.75	2.54
98	1	2	0	−1	0.65	1.73	2.53
99	1	2	1	0	0.79	1.83	2.4
100	1	2	2	2	1.26	1.64	1.22
101	2	0	0	−1	2.26	2.88	3.62
102	2	0	−1	0	2.92	3.66	4.39
103	2	0	0	2	1.48	1.92	2.33
104	2	0	1	1	1.28	2.04	2.62
105	2	0	2	0	1.54	2.46	2.83
106	2	−1	0	0	2.88	3.36	4.11
107	2	−1	−1	2	3.54	3.85	4.17
108	2	−1	0	1	2.62	3.13	3.82
109	2	−1	1	0	2.16	2.71	3.39
110	2	−1	2	−1	2.16	2.59	2.88
111	2	0	0	2	1.48	1.92	2.33
112	2	0	−1	1	2.66	3.34	3.96
113	2	0	0	0	2	2.76	3.57
114	2	0	1	−1	1.8	2.48	3.1
115	2	0	2	0	1.54	2.46	2.83
116	2	1	0	1	0.86	1.59	2.26
117	2	1	−1	0	1.78	2.65	3.45
118	2	1	0	−1	1.38	2.21	3.02
119	2	1	1	0	0.92	1.85	2.51
120	2	1	2	2	0.66	1.18	0.97
121	2	2	0	0	0.24	1.08	1.89
122	2	2	−1	−1	0.9	1.78	2.64
123	2	2	0	0	0.24	1.08	1.89
124	2	2	1	2	−0.22	−0.02	−0.03
125	2	2	2	1	0.56	1.28	1.24

4. Mathematical Model Development

Angular distortion can be expressed in the form of

$$Y = f [\theta, t, F, S]$$

where, Y = Response function e.g., Angular Distortion, degrees, θ = Angle of the nozzle, degrees° t = Time gap between passes, min, F = Wire feed rate, m/min and S = Welding speed, cm/min

The response surface for k factors is represented by the second order polynomial (regression) equation, which is:

$$Y = b_0 + \sum_{i=1}^k b_i X_i + \sum_{i,j=1}^k b_{ij} X_i X_j + \sum_{i=1}^k b_{ii} X_i^2 \quad (3)$$

where b_0 is the free term of the regression equation, the coefficient $b_1, b_2 \dots b_k$ are linear terms, the coefficients $b_{11}, b_{22}, \dots b_{kk}$ are quadratic terms and coefficients $b_{12}, b_{13}, \dots b_{k-1,k}$ are the interaction terms.

The values of these coefficients were calculated using the statistical programme Quality America DOE PC IV. The regression coefficients' values indicate to what extent the control factors have a quantifiable impact on the response. Without compromising much accuracy, the less significant coefficients are removed together with the replies to which they are linked. The student's t -test is used to accomplish this. According to this test, the coefficient becomes significant when the estimated value of t pertaining to it exceeds

the usual tabulated value for the probability criteria fixed at 0.75; otherwise, it becomes insignificant [63–67]. Only the most significant coefficients were used to generate the final mathematical models. Table 4 shows that Calculation of variance for testing the adequacy of the model.

The foregoing analysis yielded the following mathematical models:

$$\alpha_2 = 1.38 + 0.09 \times \theta - 0.18 \times t - 0.27 \times F + 0.11 \times \theta^2 + 0.23 \times F^2 - 0.35 \times \theta \times t + 0.21 \times \theta \times F - 0.13 \times \theta \times S + 0.26 \times t \times F \quad (4)$$

$$\alpha_3 = 2.23 + 0.22 \times \theta - 0.27 \times F - 0.08 \times t^2 + 0.25 \times F^2 - 0.10 \times S^2 - 0.34 \times \theta \times t - 0.19 \times \theta \times F - 0.11 \times \theta \times S + 0.26 \times t \times F - 0.09 \times t \times S \quad (5)$$

$$\alpha_4 = 3.15 + 0.21 \times \theta - 0.27 \times F + 0.10 \times t^2 + 0.15 \times F^2 - 0.19 \times S^2 - 0.32 \times \theta \times t - 0.20 \times \theta \times F - 0.12 \times \theta \times S + 0.20 \times t \times F - 0.14 \times t \times S \quad (6)$$

Table 4. Calculation of variance for testing the adequacy of the model.

Parameter	Factors (SS)	df	Lack of Fit (SS)	Df	Error Terms (SS)	df	F Ratio	R Ratio	Whether the Model Is Adequate
(α_2)	19.34	14	5.45	10	1.08	6	3.02	7.67	Adequate
(α_3)	21.293	14	7.67	10	1.36	6	3.37	6.68	Adequate
(α_4)	19.01	14	8.23	10	2.04	6	2.026	4.02	Adequate

5. Neural Network Model Development

In many engineering fields, artificial neural networks (ANN) are one of the most astonishing statistical modelling techniques currently in use for simulating complicated interactions that are challenging to represent using traditional models. Neural networks' extraordinary data-handling abilities, which also include nonlinearity, high parallelism, fault and noise tolerance, as well as learning and generalisation capabilities [37], are what make them so alluring. The use of artificial neural networks in the modelling and monitoring of welding processes has sparked a never-ending surge in research interest. The goal is to use ANN to create models that forecast angle distortion for time gaps of two, three, and four passes.

5.1. Neural Network Model Development

In this case, a feed-forward back-propagation network was utilised to forecast angular distortion. A multi-facet network was used because it has ability to solve complex nonlinear problems by employing hidden layers. Multi-facet network had three layers: an input layer for handling input data information, an output layer for providing responses, and a hidden layer for handling information and yielding output. The hidden layers enhance the separation capacity of the network. Hence it is called as multi-facet network. To reduce error, this network uses the network training function, which uses gradient descent to update weights and bias values. At the learning step, information from the tests, such as welding parameters and angular distortion values, was passed on to a network. During network learning, the output of the network was compared to the desired output, and the connector weights within the network were adjusted to lessen the discrepancy. The error was propagated backwards through the network based on the back-propagation learning process, and weights were changed. Learning will come to an end in this iterative learning system after a suitable mistake has been acquired. The prepared network responds in accordance with the knowledge it has learned when new data (beyond training) is supplied.

5.2. Network Training

The neural network model was built using a total of 125 experimental data sets. The data should be standardised to alleviate the training issue and balance the value of the training process. Learning will be delayed or nonexistent if the sigmoid function is saturated. To circumvent this, the data is standardised between marginally offset values like 0.1 and 0.9 rather than 0 and 1. The normalised input and output data set values for each row are calculated using Equation (7).

$$x_i = 0.1 + 0.8 \left(\frac{z_i - z_{\min}}{z_{\max} - z_{\min}} \right) \quad (7)$$

where

X_i = Normalized input/output value

Z_i = Actual input/output value

Z_{\max} = Maximum input/output value

Z_{\min} = Minimum input/output value

The data must be separated into training and testing data in order to calculate the ratio between the two. For this, there is no particular guideline. However, the proportions can be expressed as 90:10%, 85:15%, 80:20%, and 70:30%. In this study, the 125 experimental data points were divided into three categories: training, testing, and validation. As a result, 87, 19, and 19 experimental samples were used for training, testing, and validation, respectively, out of a total of 125 samples.

The network structure was built using a trial-and-error approach. The trial-and-error process was carried out by varying the number of nodes in the hidden layer of the network structure. However, for the hidden layer, depending on the complexity of the mapping, the available computer memory, the computation time, and the desired impact on data control, it was feasible to view the network with any number of nodes. An excessive number of nodes could waste computer memory and calculation time, while a small number of nodes would not provide the required data control effect [38]. The recommended number of nodes for the hidden layer in this work is “ $n/2$,” “ $1n$,” “ $2n$,” and “ $2n + 1$,” with “ n ” being the number of input nodes. Because there are four choice factors in this study, the optimal number of hidden layer nodes is $4/2 = 2$, $1(4) = 4$, $2(4) = 8$, and $2(4) + 1 = 9$. This study’s trial and error was limited to four networks: 4-2-3, 4-4-3, 4-8-3, and 4-9-3. MATLAB 8.5 was used to create the networks. Figure 6 hidden layer network with nine neurons.

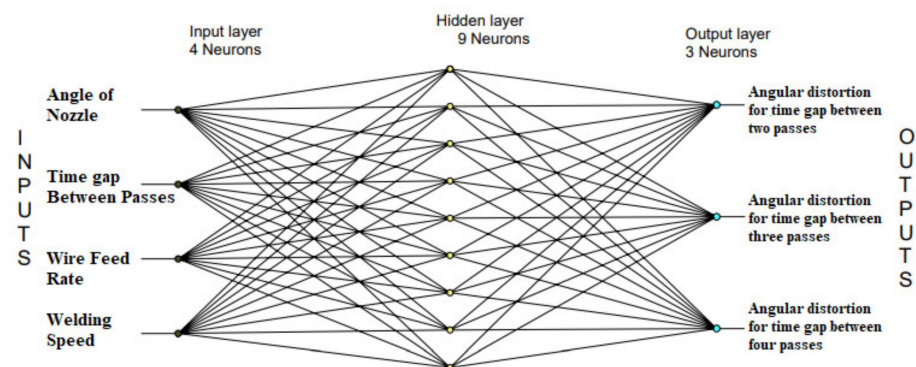


Figure 6. Network 4-9-3 with nine neurons.

The learning rate and momentum parameters must be set after the network architecture has been completed. The extent of the weight and bias changes that take place during learning is controlled by the learning rate, a preliminary parameter. Its value is 0.3 because if it is too high, the system will either not be able to determine the right answer or completely diverge. It will take the system a substantial amount of the day to reach

a final solution if it is too low. The system is prevented from reaching a local minimum or saddle point by the momentum parameter. In essence, it adds the value “m” from the previous update to the current one. The system’s convergence is accelerated by a high momentum parameter, but if it is set too high, the minimum value may be exceeded. By doing this, future system instability will be avoided. If the momentum parameter is set too low, the system’s setup may be slowed. As a result, the momentum parameter is set at 0.05 in this study.

For network training, the Levenberg–Marquardt (LM) algorithm was utilised. The LM algorithm uses an error corrective learning rule. In the LM algorithm, operating phases make use of forward connections, whereas learning phases make use of backward links. Because it is a Hessian-based method and allows the network to learn more delicate characteristics of a complicated mapping, the LM algorithm is preferred over the others. The training phase of the LM method converges quickly as the solution is approached because the Hessian vanishes at the solution. During training, the inputs from the neurons were weighted. Using a tan -sigmoid transfer function, the weight input and bias sum were changed. In a similar manner, the output of the final hidden layer was tailored using a suitable weight, and the sum of the tailored output signal was afterwards modified using a tan—sigmoid transfer function. The complete item was gathered at the output layer. Using a transfer function, the sum of the weight input and bias was modified.

5.3. Testing the Network

The effectiveness of the ANN model for forecasting angular distortion with time gaps of two, three, and four passes was investigated using four networks: 4-2-3, 4-4-3, 4-8-3, and 4-9-3. During each training session, a set of inputs from the training sample (‘Xi’) was presented, and the results (‘Oi’) were produced. The network model’s projected value is then compared to the actual value ‘di.’ To evaluate the results, the mean squared error (MSE) between “di” and “Oi,” as stated in Equation (8), was utilised. The algorithm’s main objective was to reduce the mean squared error for all experimental data. [39,40].

$$\text{MSE} = (d_i - O_i)^2 \quad (8)$$

5.4. Network Analysis

For each network, the following must be looked at to figure out how well it can predict angular distortion with time gaps of two, three, and four passes.

1. Performance analysis
2. Error analysis
3. Regression analysis

Performance analysis [41,42] is used to determine MSE. When MSE is near zero, the network has been carefully considered the best. During the error investigation, the percentage error between the predicted and experimental values was computed. The network has a high level of accuracy in predicting angular distortion if the percentage error is less than 5%. When performing a regression analysis, the correlation coefficient is calculated. This approach aids in the identification of the link between expected and observed values [43].

The performance graph of the network 4-2-3 is shown in Figure 7. The network was trained for 175th epochs. After 175th epochs, no more progress was found. At the 169th epoch, the best value was 0.0053773. The percentage error between the observed and anticipated values for angular distortion with time gaps of two, three, and four passes is shown in Figures 8–10 for the network 4-2-3. Any model is considered to be accurate if the percentage of error between the predicted and experimental values is reasonably low. For a good measurement system, the accuracy error should be within 5% and the precision should be within 10% Figures 8 and 9 depicts percentage of error for angular distortion showing time gap between two passes. The error percentage is between 0 to 0.5% which depicts that the network 4-2-3 is able to predict angular distortion with good accuracy.

The following Equation (9) is used to calculate the neural network model's error percentage.

$$\left(\frac{\text{Observedvalue} - \text{Predictedvalue}}{\text{Observed value}} \right) \times 100 \quad (9)$$

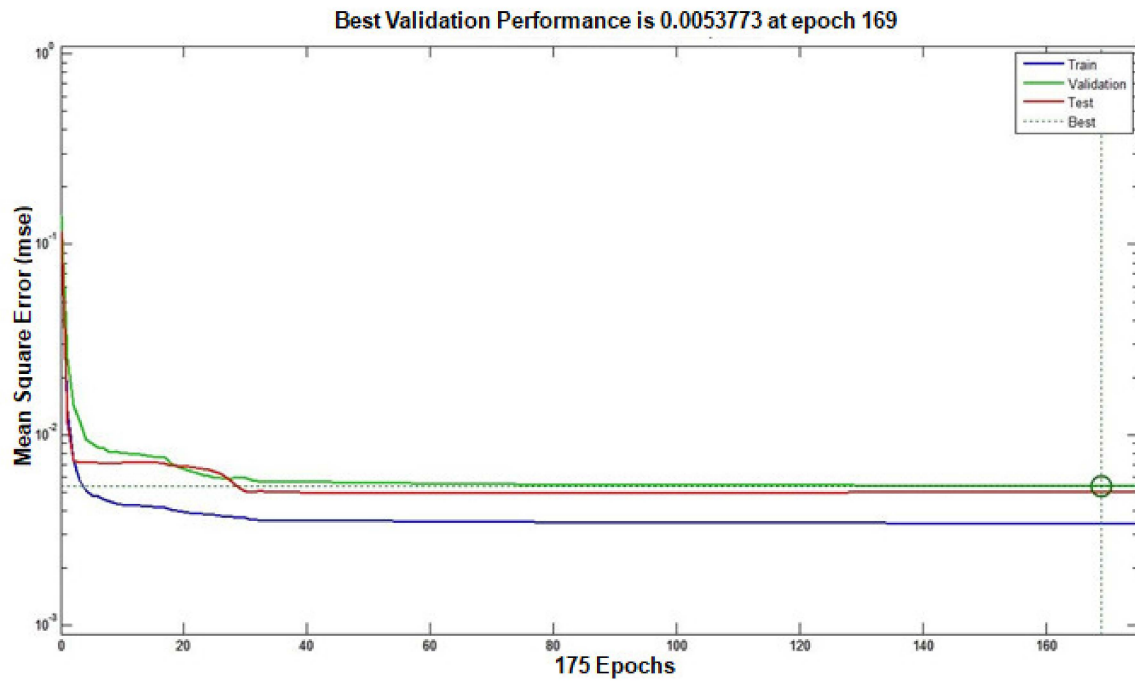


Figure 7. Network 4-2-3 performance graph for angular distortion showing time gap between two, three and four passes.

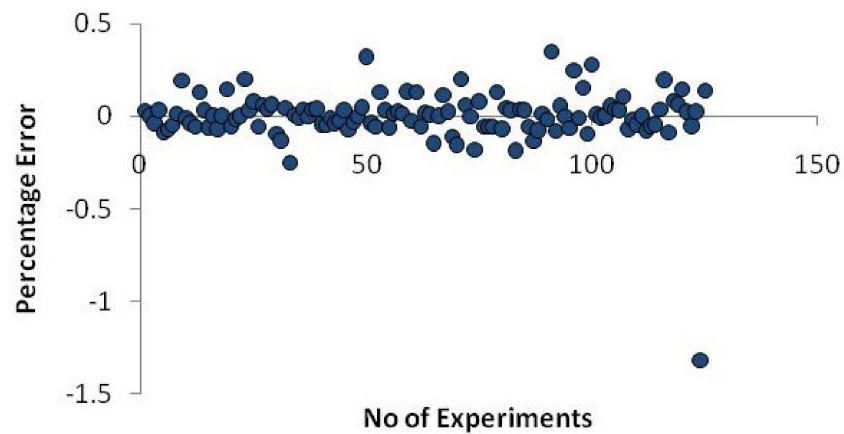


Figure 8. Network 4-2-3 error graph for angular distortion showing time gap between two passes.

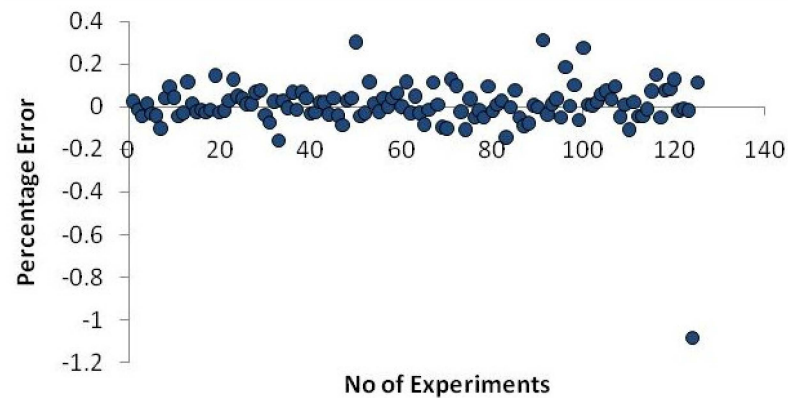


Figure 9. An angular distortion network 4-2-3 error graph demonstrating the time gap between two passes.

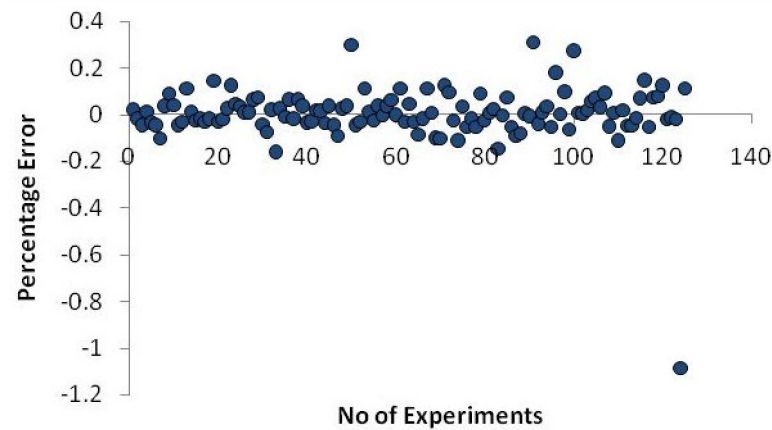


Figure 10. Network 4-2-3 error graph for angular distortion showing time gap between four passes.

According to the Figure 10, the error percentage ranges between -1.5% and $+0.5\%$ for angular distortion with a time gap between two passes and -1.2% to 0.3% for angular distortion with a time gap between three and four passes. The percentage error is within 5% . Hence, the network model is able to predict the angular distortion with reasonable accuracy.

The regression graph of network 4-2-3 is shown in Figure 11. The regression analysis helps determine the correlation connecting the predicted and observed values. The R value of “0” implies an arbitrary correlation, whereas an R value of “1” implies a close correlation. From the regression graph, it can be inferred that the regression coefficients for training, testing, and validation are 0.89, 0.92, and 0.88, respectively. This implies that further improvement in the result is possible by training with other suitable networks. Hence, the network 4-2-3 is not suitable for predicting angular distortion with a time gap between two, three, and four passes.

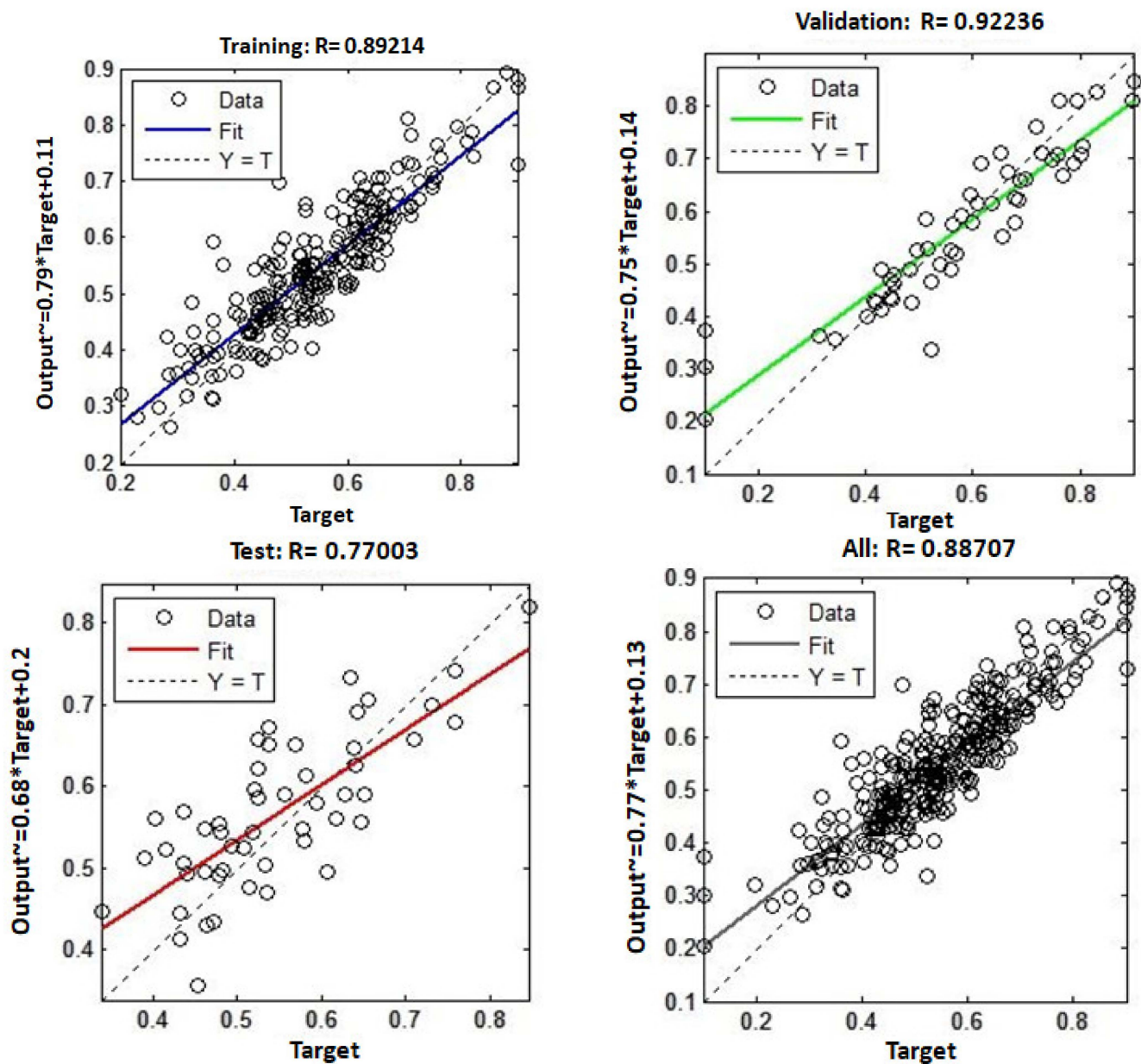


Figure 11. Regression graph of network 4-2-3 for angular distortion with time gap between two, three and four passes.

Figure 12 depicts the network's 4-4-3 performance graph. 216th epochs were used to train the network. After 210th epochs, there was no noticeable progress. At the 210th epoch, the best result was 0.00055323.

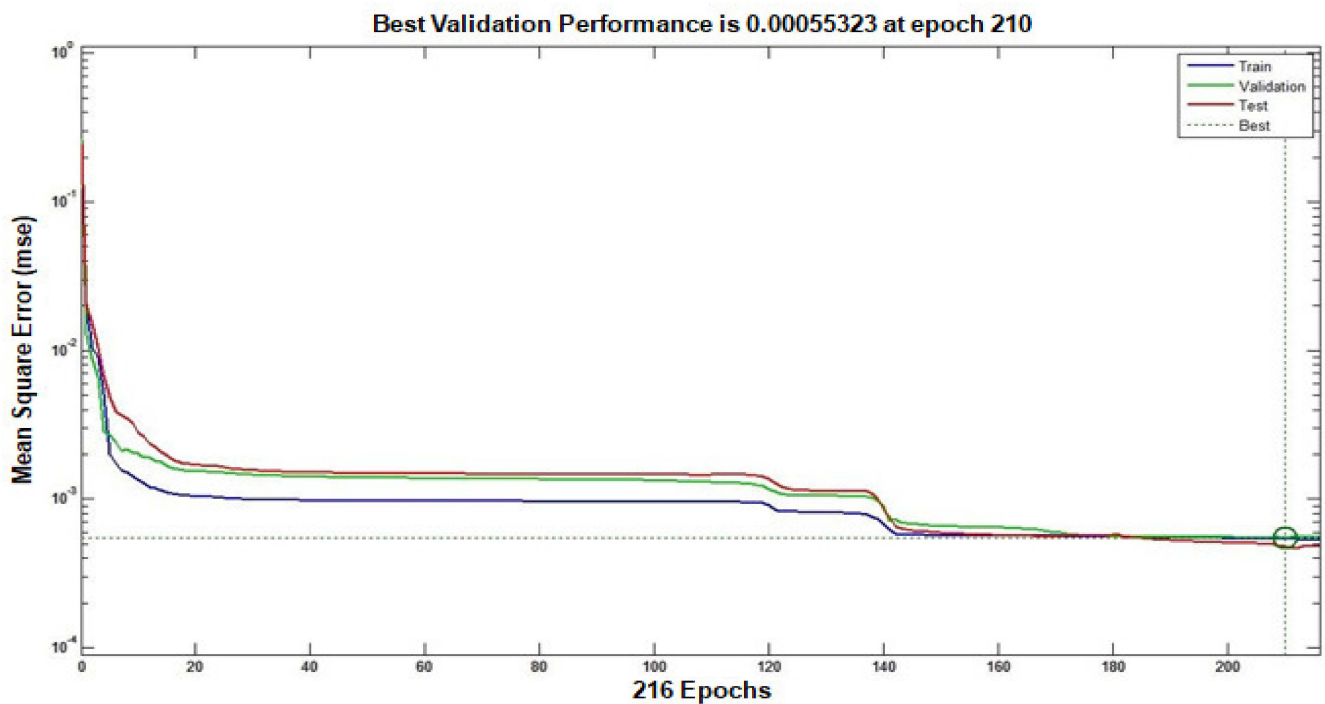


Figure 12. Performance graph of network 4-4-3 for angular distortion with time gap between two, three and four passes.

Figure 13 depicts the regression graph for the network 4-4-3. For training, validation, and testing, R values of 0.98503, 0.9809, and 0.9908 are obtained. The R value is near one, indicating that the observed and anticipated values are closely related.

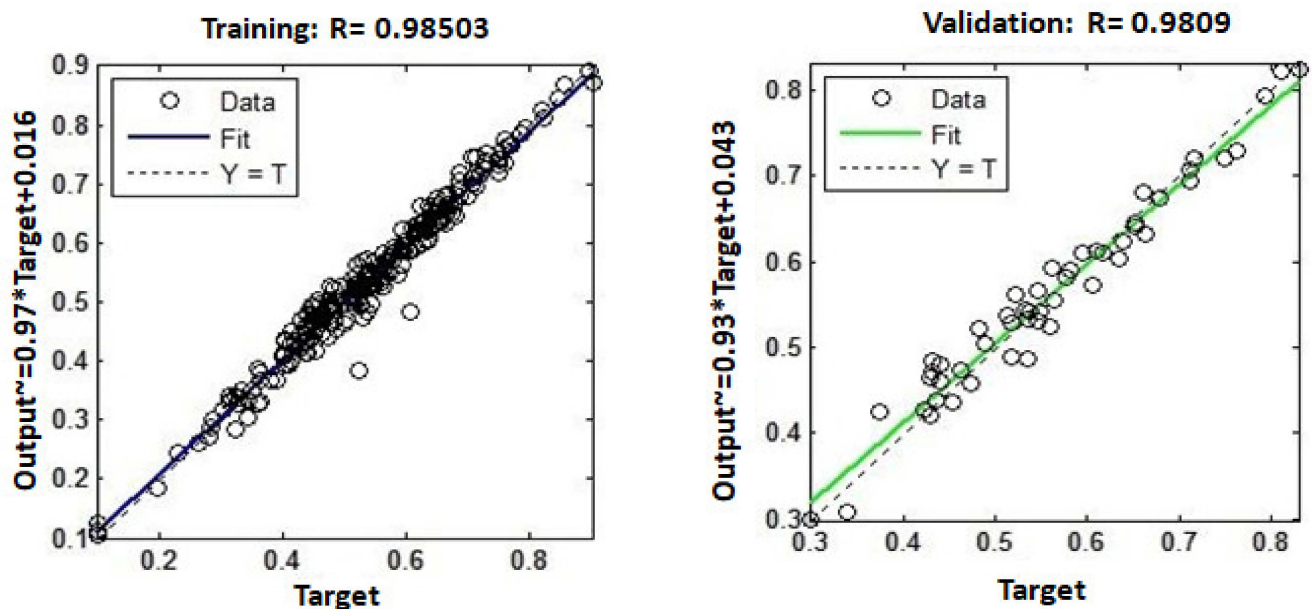


Figure 13. Cont.

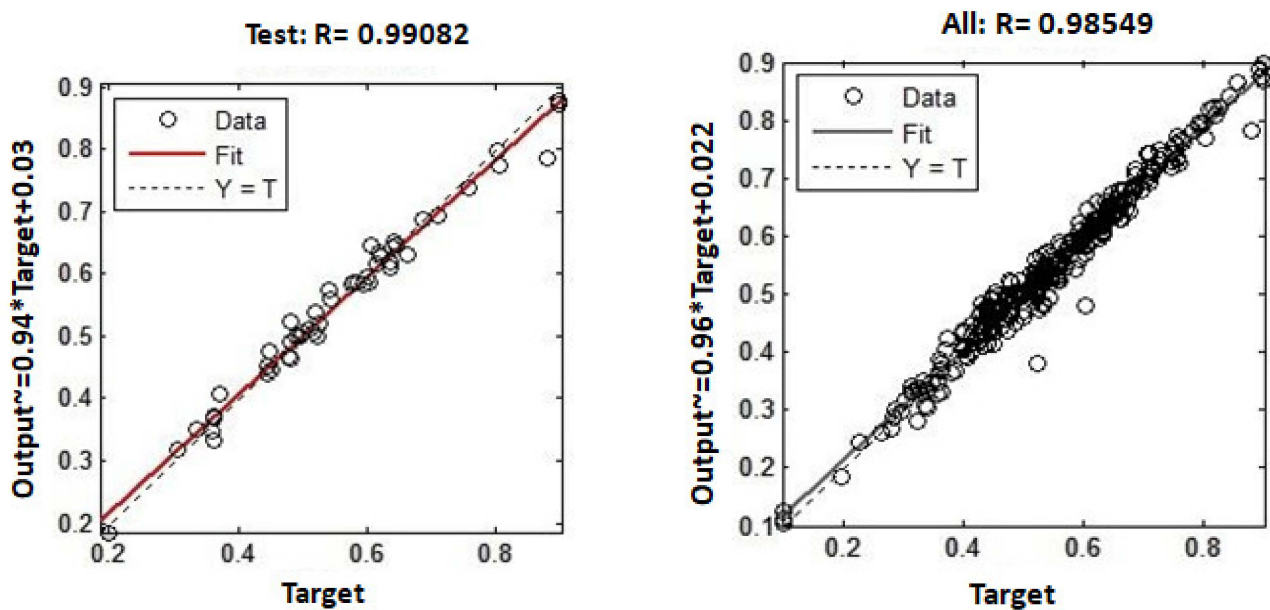


Figure 13. Regression graph for angular distortion with time gap between two, three and four passes pertaining to network 4-4-3.

The % error for angular distortion is shown in Figures 14–16 for time gaps of two, three, and four passes, respectively. The error percentage for angular distortion varies from -5 to $+6\%$, as shown in the figures. As a result, this network's prediction ability is lower than that of network 4-2-3. Although the R value is near one, the error percentage is higher, implying that the network is unsuitable for forecasting angular distortion in all three circumstances.

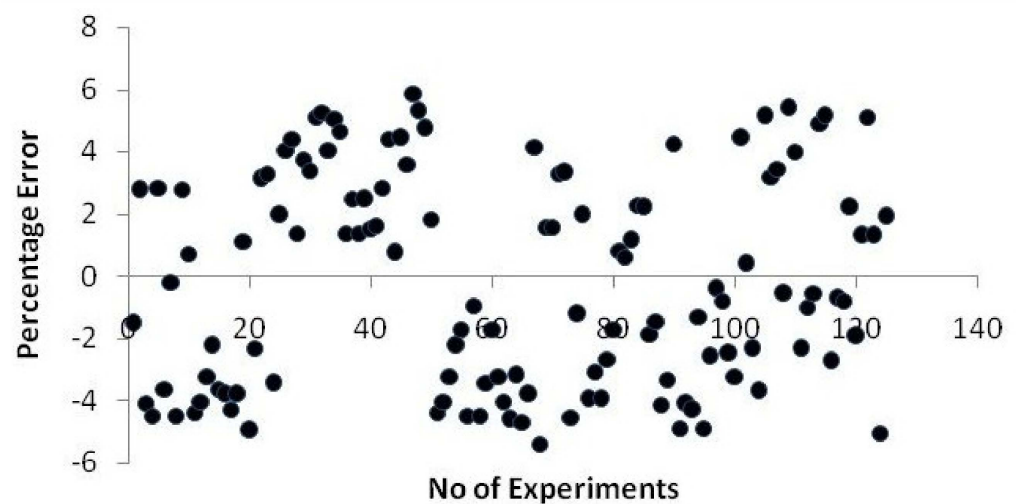


Figure 14. Network 4-4-3 error graph for angular distortion with a time gap between two passes.

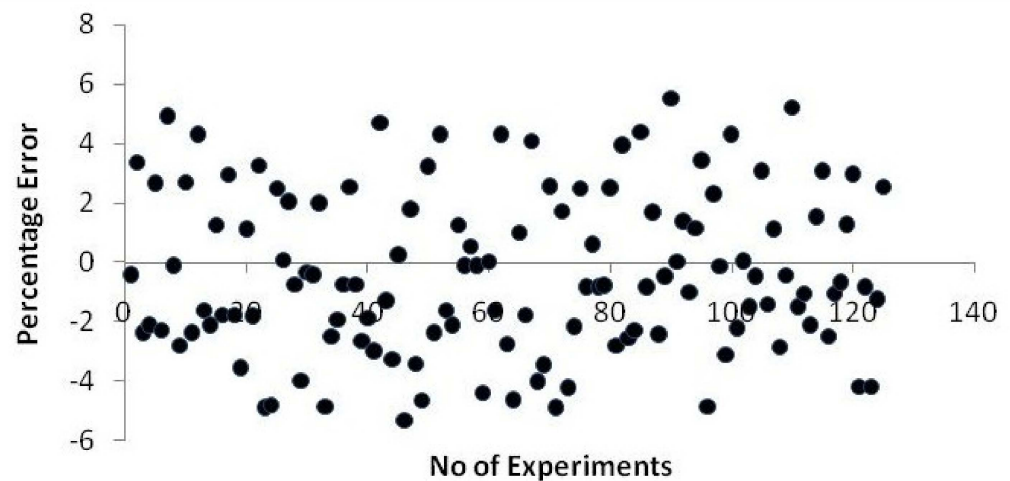


Figure 15. The network 4-4-3 error graph for angular distortion with a time gap between three passes.

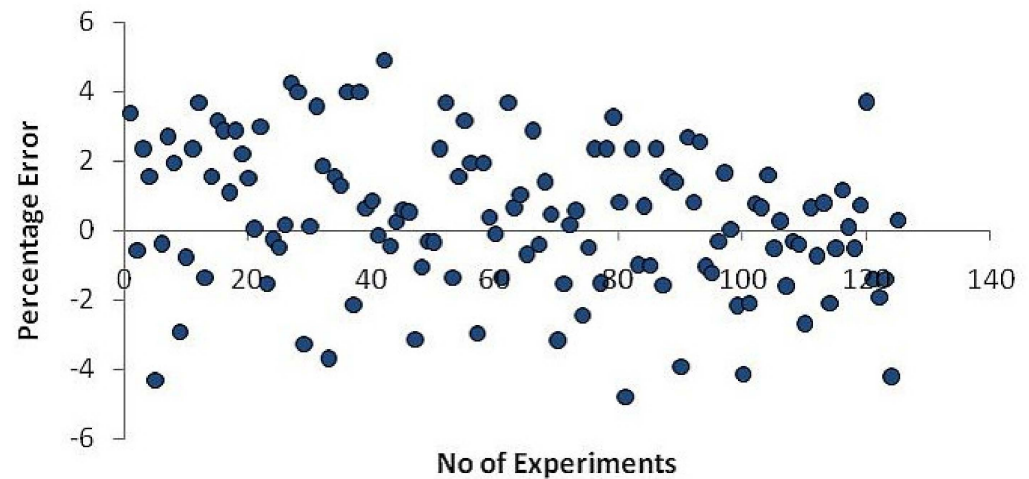


Figure 16. Network 4-4-3 error graph for angular distortion with a time gap between four passes.

Figure 17 depicts the performance of the network 4-8-3. 427th epochs were used to train the network. There has been no improvement in training after 427th epochs. As a result, the training was halted. At the 421st epoch, the best value was 3.5427×10^{-7} . In Figure 18, the network's regression graph is depicted. The R values for training, testing, and validation have been calculated from the graph and is 1, 0.99, and 0.99, respectively. Because R is close to 1, the observed and predicted values of angular distortion with time gaps of two, three, and four passes are closely related for training, testing, and validation.

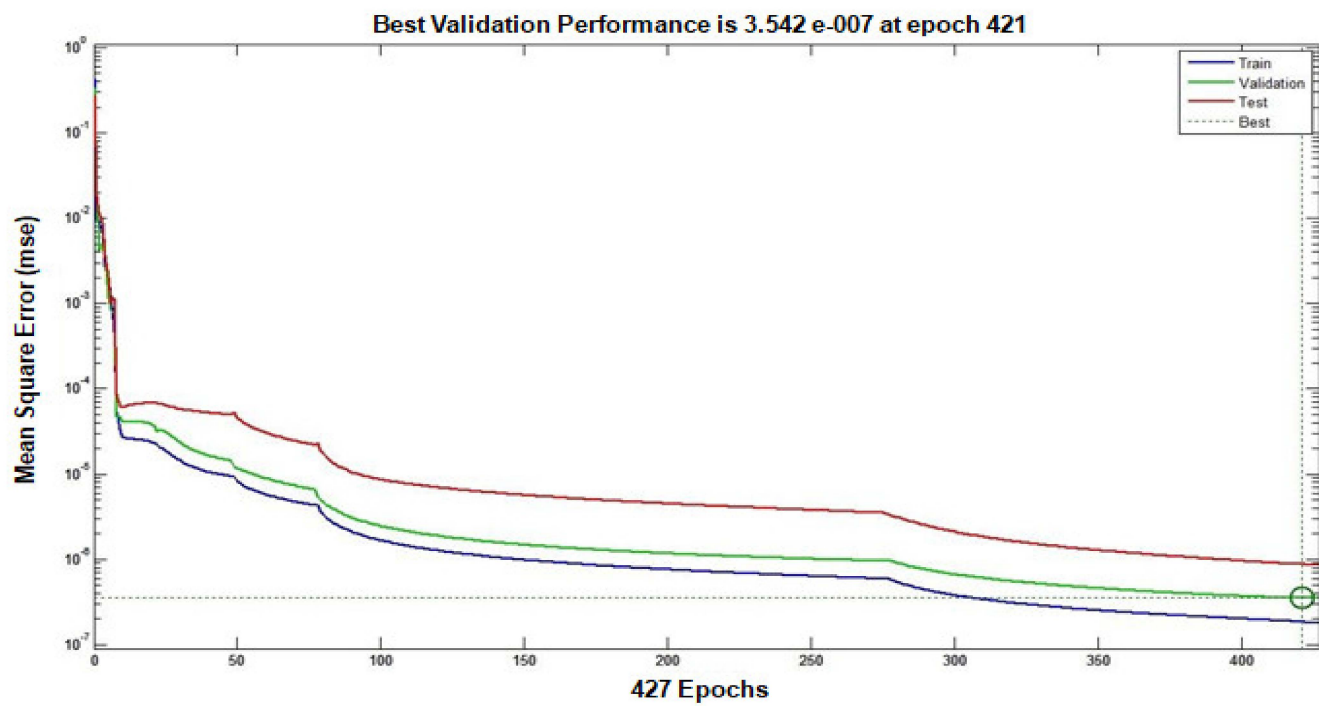


Figure 17. Performance graph of network 4-8-3 for angular distortion with time gap between two, three and four passes.

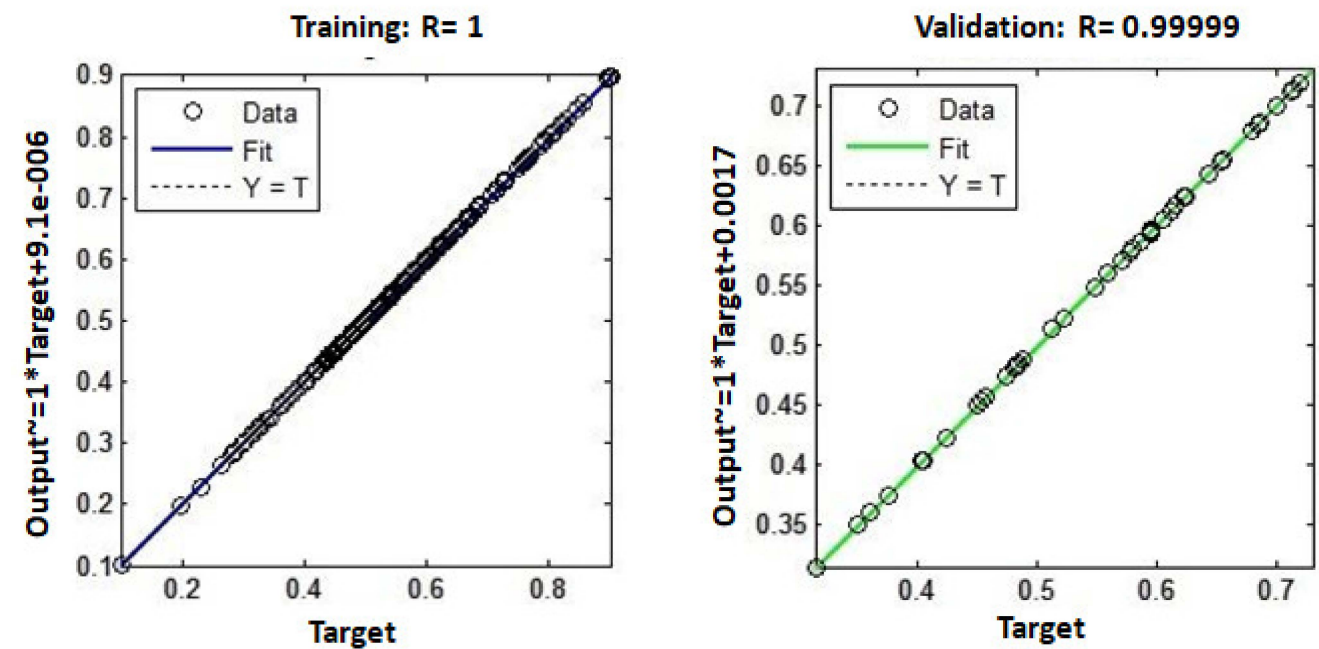


Figure 18. Cont.

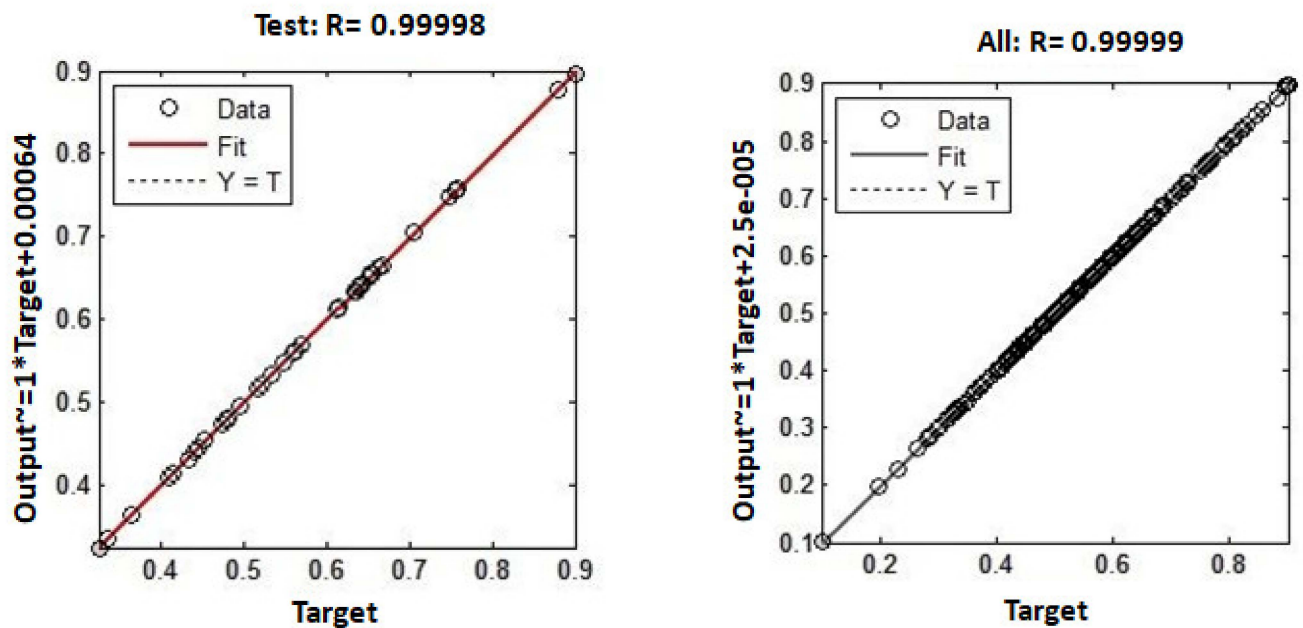


Figure 18. Regression graph of network 4-8-3 for angular distortion with time gap between two, three and four passes.

Figures 19–21 show the % error for angular distortion for the network 4-8-3 with time gaps of two, three, and four passes. The error percentage for angular distortion varies between -0.8 and 0.5 percent for two passes, -1 to $+1.3$ percent for three passes, and -1.1 to 0.3 percent for four passes, according to the results. This network has a low rate of error, an R value near 1, and an MSE near 0. In comparison to the other two networks, the network's prediction capability is high.

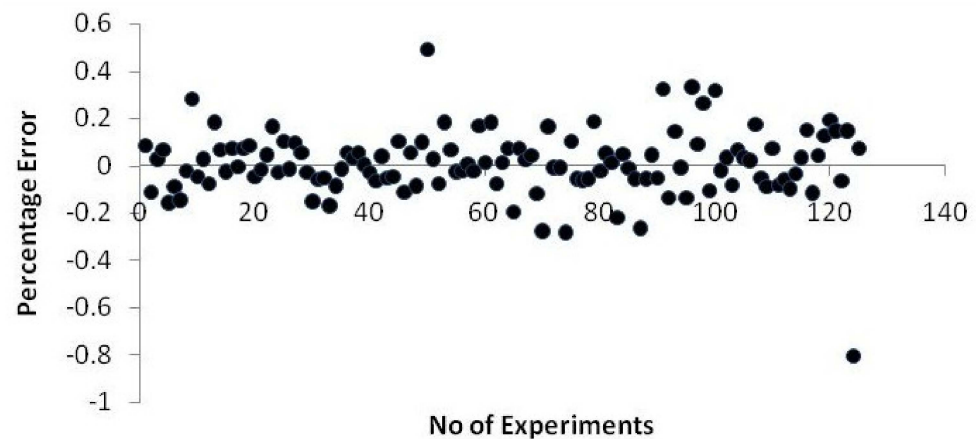


Figure 19. Error graph of network 4-8-3 for angular distortion with time gap between two passes.

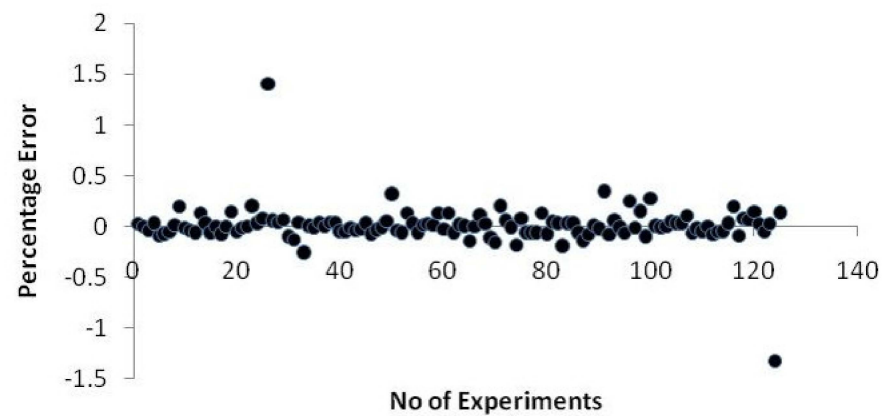


Figure 20. Error graph of network 4-8-3 for angular distortion with time gap between three passes.

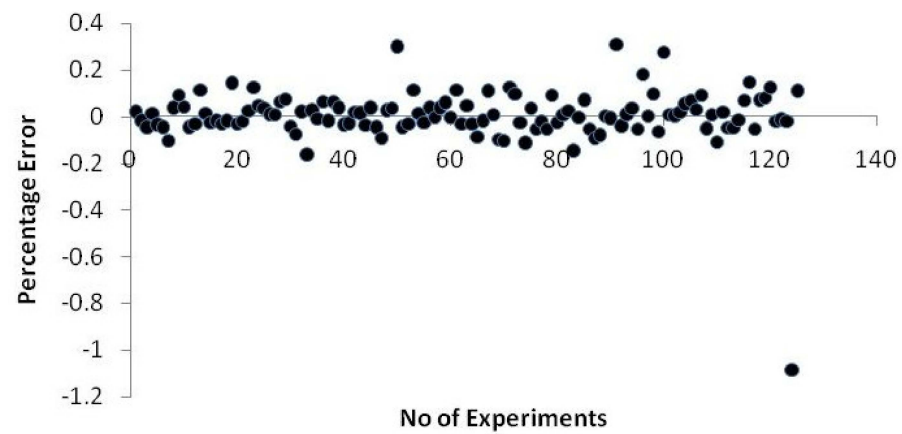


Figure 21. Error graph of network 4-8-3 for angular distortion with time gap between four passes.

Figure 22 depicted the network's performance graph. The training was carried out for 1000 iterations, with an MSE of 6.1041×10^{-8} observed at the 1000th epoch, as shown in the figure.

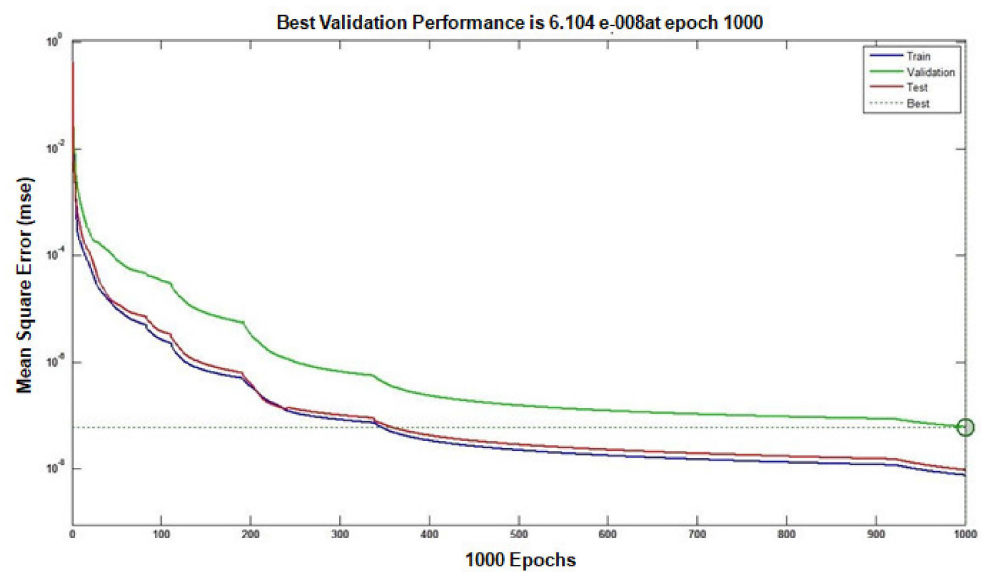


Figure 22. Performance graph of network 4-9-3 for angular distortion between two, three and four passes.

Figures 23–25 show the percentage of difference between what was seen and what was expected for angular distortion with time gaps of two, three, and four passes.

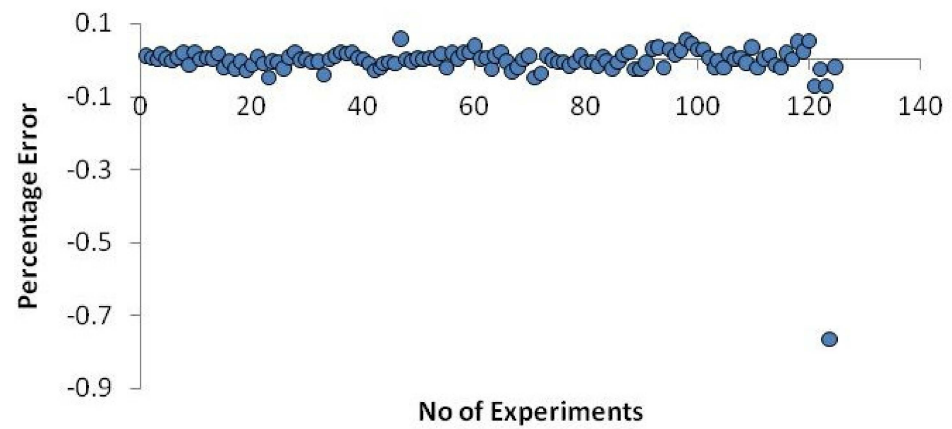


Figure 23. Error graph of network 4-9-3 for angular distortion with time gap between two passes.

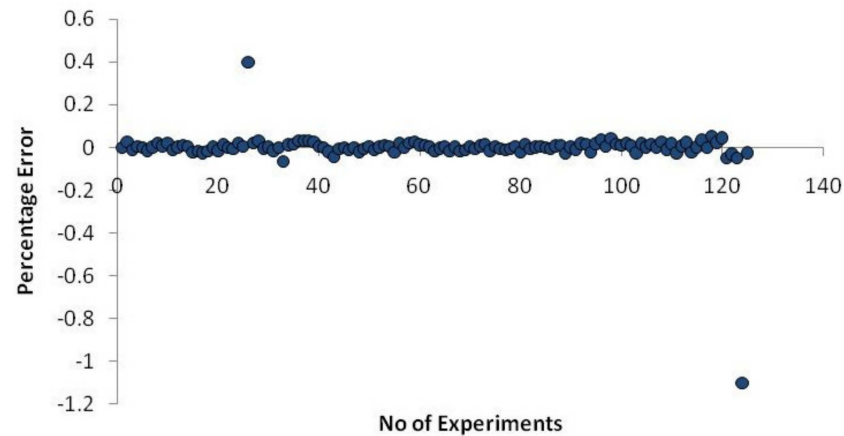


Figure 24. Error graph of network 4-9-3 for angular distortion with time gap between three passes.

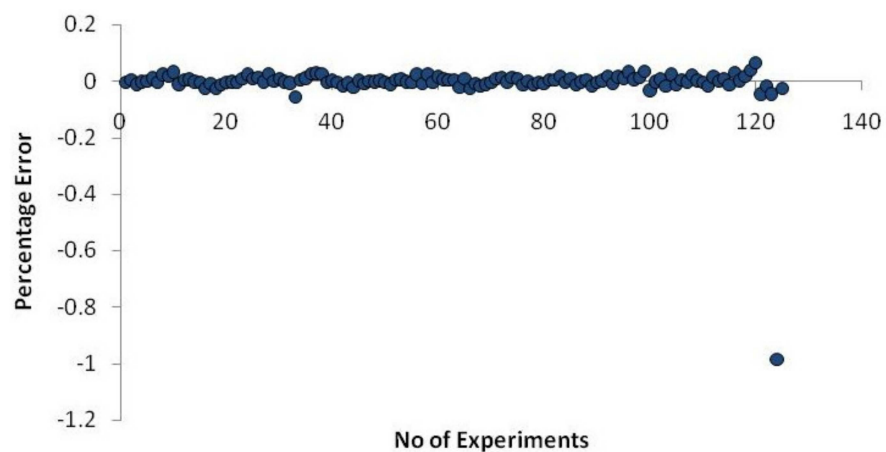


Figure 25. Error graph of network 4-9-3 for angular distortion with time gap between four passes.

The error percentage of angular distortion varied from -0.7% to $+0.1\%$, -1% to $+0.4\%$, and -0.9% to $+0.1\%$ for time gaps between two, three, and four passes, respectively, as shown in the figures.

Figure 26 depicts the network 4-9-3's regression graph. For training, testing, and validation, the R value of the network is "1". This demonstrates a very close relationship between observed and projected values.

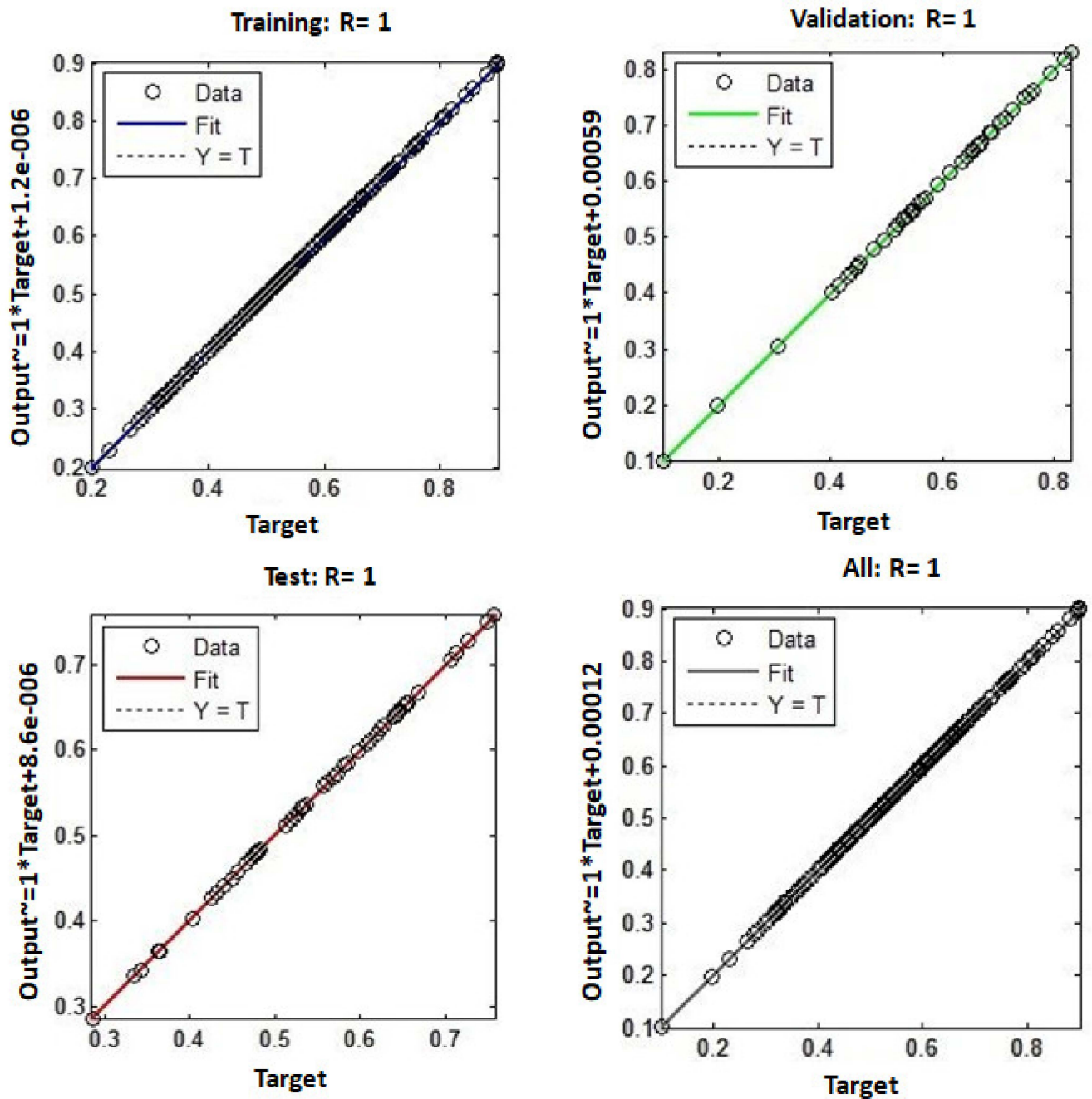


Figure 26. Regression graph of network 4-9-3 for angular distortion with time gap between two, three and four passes.

In comparison to the networks 4-2-3, 4-4-3, and 4-8-3, the network 4-9-3 has a very low MSE value, a regression coefficient of "1" for training, testing, and validation, and an error percentage of less than 2% for angular distortion between two, three, and four passes. As a result, the network (4-9-3) predicts angular distortion with high accuracy.

6. Confirmation of Results and Discussion

The results were confirmed by doing further tests with the identical experimental setup and comparing the results to those predicted by the network 4-9-3. The process variables consider for the Validation tests are combination of parameters that were not considered in design matrix of 125 trial runs. Tables 5–7 shows the results of validation tests.

Table 5. Results of Validation Tests.

Test. No	Input Values of Process Variables for which Validation Tests Were Conducted			
	θ°	T	F	S
1	70	10	5.5	10.2
2	80	15	5.75	10.8
3	90	20	6	8.4

Table 6. Continued.

Angular Distortion in Degrees for Time Gap between Two Passes			Angular Distortion in Degrees for Time Gap between Three Passes		
O.V	P.V	Error%	O.V	P.V	Error%
1.38	1.397	−1.21	1.33	1.321	0.68
1.83	1.797	1.83	2.09	2.115	−1.18
2.1	2.056	2.14	2.98	2.947	1.12
Mean Error		0.92	Mean Error		0.20

Table 7. Continued.

Angular Distortion in Degrees for Time Gap between Four Passes		
O.V	P.V	Error%
2.18	2.196	−0.72
2.50	2.466	1.37
3.03	2.979	1.71
Mean Error		0.79

O.V—The process parameters observed value as determined by experiment. P.V—derived from the ANN model, predicted value of the process parameter.

According to the validation tests, network 4-9-3 was able to accurately forecast angle distortion with time gaps of three, four, and five passes. The deviation between the observed value and the predicted value is very minimal. From the table deviation is observed less than 5%. The mean error was found to be 0.92 percent, 0.20 percent, and 0.79 percent, respectively, for angular distortion with time gaps of two, three, and four passes. This suggests that compared to the other three networks, the model based on network 4-9-3 is more successful at predicting angular distortion with time gaps between two, three, and four passes (4-2-3, 4-4-3, and 4-8-3). More than 95% of predictions are correct.

7. Conclusions

Based on the findings, the following conclusions can be drawn:

1. In the gas metal arc welding technique, the structural steel studied in this work had good weld quality to achieve products of high quality. The products obtained from the GMAW of structural steel plate meets the required strength and free from angular distortion, which are the good weld quality criteria. As a result, it can be used in residential, commercial, and aviation hangar construction, as well as for construction purposes in metro stations, stadiums, and bridges.
2. The fractional factorial-based 125 experimental runs were successful in collecting the data needed to create a neural network model.

3. Validation experiments were carried out to ensure the network's accuracy in forecasting angular distortion. The mean error for angular distortion with time gaps of two, three, and four passes was determined to be 0.92 percent, 0.20 percent, and 0.79 percent, respectively. This indicates that the model based on network 4-9-3 is more effective in forecasting angular distortion with time gaps between two, three, and four passes than the other three networks (4-2-3, 4-4-3, and 4-8-3). Prediction accuracy is more than 95 percent.
4. The result shows that for training data, testing data, validation data, and all data, a correlation coefficient of $R = 1$ was found. Henceforth, there exists a good correlation between the observed and the predicted models.
5. According to the study, different angular distortion values can be predicted by varying the hidden layer's node count and applying a similar training method. The butt weld plate production process can be controlled using the neural network model developed in this paper to achieve the desired weld quality.
6. The neural network model developed in this study can be used to manage the welding cycle in structural steel weld plates to achieve the best possible weld quality with the least amount of angular distortion.
7. It is possible to develop a neural model for the prediction of angular distortion in thinner materials. As far as thinner materials are concerned, the gas tungsten arc welding process will be more appropriate because GTAW welds are preferable for thinner metals because they result in accurate and clean welds. Larger jobs requiring longer, continuous runs and thick metals respond well to GMAW welding.

Author Contributions: Conceptualisation K.M.E. and R.S.; methodology, R.S.; software, E.P.V.; validation, R.S.; formal analysis, A.A.; investigation, M.B.; resources, R.S.; data curation, R.S.; writing—original draft preparation, R.S.; writing—review and editing, K.M.; visualisation, M.B.; supervision, K.M.E.; project administration, K.M.E.; funding acquisition, M.B. All authors have read and agreed to the published version of the manuscript.

Funding: This research is supported by the Structures and Materials (S&M) Research Lab of Prince Sultan University and the authors acknowledge the support of Prince Sultan University for paying the article processing charges (APC) of this publication.

Data Availability Statement: Not applicable.

Conflicts of Interest: The authors declare no conflict of interest.

References

1. Shen, J.; Gonçalves, R.; Choi, Y.T.; Lopes, J.G.; Yang, J.; Schell, N.; Kim, H.S.; Oliveira, J.P. Microstructure and mechanical properties of gas metal arc welded CoCrFeMnNi joints using a 410 stainless steel filler metal. *Mater. Sci. Eng. A* **2022**, *857*, 144025. [\[CrossRef\]](#)
2. Shen, J.; Gonçalves, R.; Choi, Y.T.; Lopes, J.G.; Yang, J.; Schell, N.; Kim, H.S.; Oliveira, J.P. Microstructure and mechanical properties of gas metal arc welded CoCrFeMnNi joints using a 308 stainless steel filler metal. *Scr. Mater.* **2023**, *222*, 115053. [\[CrossRef\]](#)
3. Shen, J.; Agrawal, P.; Rodrigues, T.A.; Lopes, J.G.; Schell, N.; He, J.; Zeng, Z.; Mishra, R.S.; Oliveira, J.P.; Shen, J.; et al. Microstructure evolution and mechanical properties in a gas tungsten arc welded Fe₄₂Mn₂₈Co₁₀Cr₁₅Si₅ metastable high entropy alloy. *Mater. Sci. Eng. A* **2023**, *867*, 144722. [\[CrossRef\]](#)
4. Masubuchi, K. *Analysis of Welded Structures*; Pergamon Press: Oxford, UK, 1986. [\[CrossRef\]](#)
5. Choobi, M.S.; Haghpanahi, M.; Sedighi, M. Prediction of welding-induced angular distortions in thin butt-welded plates using artificial neural networks. *Comput. Mater. Sci.* **2012**, *62*, 152–159. [\[CrossRef\]](#)
6. Adamczuk, P.C.; Machado, I.G.; Mazzaferro, J.A.E. Methodology for predicting the angular distortion in multi-pass butt-joint welding. *J. Mater. Process. Technol.* **2017**, *240*, 305–313. [\[CrossRef\]](#)
7. Kadir, M.H.A.; Asmelash, M.; Azhari, A. Investigation on welding distortion in stainless steel sheet using gas tungsten arc welding process. *Mater. Today Proc.* **2021**, *46*, 1674–1679. [\[CrossRef\]](#)
8. Seong, W.J. Prediction and Characteristics of Angular Distortion in Multi-Layer Butt Welding. *Materials* **2019**, *12*, 1435. [\[CrossRef\]](#)
9. Ansari pour, N.; Heidari, A.; Eftekhari, S.A. Multi-objective optimization of residual stresses and distortion in submerged arc welding process using genetic algorithm and harmony search. *Proc. Inst. Mech. Eng. C J.* **2020**, *234*, 862–871. [\[CrossRef\]](#)

10. Vishvesha, A.; Pandey, C.; Mahapatra, M.M.; Mulik, R.S. On the estimation and control of welding distortion of guide blade carrier for a 660 MW turbine by using inherent strain method. *Int. J. Steel Struct.* **2017**, *17*, 53–63. [\[CrossRef\]](#)
11. Wu, C.; Wang, C.; Lee, C.; Kim, J.W. An algorithm for prediction of bending deformation induced by multi-seam welding of a steel-pipe structure. *J. Mech. Sci. Technol.* **2021**, *35*, 707–716. [\[CrossRef\]](#)
12. Zubairuddin, M.; Albert, S.K.; Mahadevan, S.; Vasudevan, M.; Chaudhari, V.; Suri, V.K. Experimental and finite element analysis of residual stress and distortion in GTA welding of modified 9Cr-1Mo steel. *J. Mech. Sci. Technol.* **2014**, *28*, 5095–5105. [\[CrossRef\]](#)
13. Venkatesan, M.V.; Murugan, N.; Prasad, B.M.; Manickavasagam, A. Influence of FCA welding process parameters on distortion of 409m stainless steel for rail coach building. *J. Iron Steel Res. Int.* **2013**, *20*, 71–78. [\[CrossRef\]](#)
14. Suman, S.; Sridhar, P.V.S.S.; Biswas, P.; Das, D. Prediction of welding-induced distortions in large weld structure through improved equivalent load method based on average plastic strains. *Weld. World* **2020**, *64*, 179–200. [\[CrossRef\]](#)
15. Rong, Y.; Zhang, G.; Huang, Y. Study of welding distortion and residual stress considering nonlinear yield stress curves and multi-constraint equations. *J. Mater. Eng. Perform. J.* **2016**, *25*, 4484–4494. [\[CrossRef\]](#)
16. Wang, C.; Kim, J.W. Numerical analysis of distortions by using an incorporated model for welding-heating-cutting processes of a welded lifting lug. *J. Mech. Sci. Technol.* **2018**, *32*, 5855–5862. [\[CrossRef\]](#)
17. Chaki, S. Neural networks based prediction modeling of hybrid laser beam welding process parameters with sensitivity analysis. *Appl. Sci.* **2019**, *1*, 1285.
18. Sudhakaran, R.; Sivasakthivel, P.S.; Subramanian, M.; Mahendran, S. Prediction of angular distortion in gas tungsten arc welded 202 grade stainless steel plates using artificial neural networks—An experimental approach. In *AIP Conference Proceedings*; AIP Publishing LLC: Melville, NY, USA, 2019; Volume 2161, p. 020050.
19. Pazooki, A.M.A.; Hermans, M.J.M.; Richardson, I.M. Control of welding distortion during gas metal arc welding of AH36 plates by stress engineering. *Int. J. Adv. Manuf. Technol.* **2017**, *88*, 1439–1457. [\[CrossRef\]](#)
20. Barclay, C.J.; Campbell, S.W.; Galloway, A.M.; McPherson, N.A. Artificial neural network prediction of weld distortion rectification using a travelling induction coil. *Int. J. Adv. Manuf. Technol.* **2013**, *68*, 127–140. [\[CrossRef\]](#)
21. Tian, L.; Luo, Y.; Wang, Y.; Wu, X. Prediction of transverse and angular distortions of gas tungsten arc bead-on-plate welding using artificial neural network. *Mater. Des.* **2014**, *54*, 458–472. [\[CrossRef\]](#)
22. Rubio-Ramirez, C.; Giarollo, D.F.; Mazzaferro, J.E.; Mazzaferro, C.P. Prediction of angular distortion due GMAW process of thin-sheets Hardox 450® steel by numerical model and artificial neural network. *J. Manuf. Process.* **2021**, *68*, 1202–1213. [\[CrossRef\]](#)
23. Banik, S.D.; Kumar, S.; Singh, P.K.; Bhattacharya, S.; Mahapatra, M.M. Distortion and residual stresses in thick plate weld joint of austenitic stainless steel: Experiments and analysis. *J. Mater. Process. Technol.* **2021**, *289*, 6944. [\[CrossRef\]](#)
24. Khoshroyan, A.; Darvazi, A.R. Effects of welding parameters and welding sequence on residual stress and distortion in Al6061-T6 aluminum alloy for T-shaped welded joint. *Trans. Nonferrous Met. Soc. China* **2020**, *30*, 76–89. [\[CrossRef\]](#)
25. García-García, V.; Mejía, I.; Reyes-Calderón, F.; Benito, J.A.; Cabrera, J.M. FE thermo-mechanical simulation of welding residual stresses and distortion in Ti-containing TWIP steel through GTAW process. *J. Manuf. Process.* **2020**, *59*, 801–815. [\[CrossRef\]](#)
26. Venkatkumar, D.; Ravindran, D.; Selvakumar, G. Finite element analysis of heat input effect on temperature, residual stresses and distortion in butt welded plates. *Mater. Today Proc.* **2018**, *5*, 8328–8337. [\[CrossRef\]](#)
27. Vasantharaja, P.; Vasudevan, M.; Palanichamy, P. Effect of welding processes on the residual stress and distortion in type 316LN stainless steel weld joints. *J. Manuf. Process.* **2015**, *19*, 187–193. [\[CrossRef\]](#)
28. Bajpei, T.; Chelladurai, H.; Ansari, M.Z. Experimental investigation and numerical analyses of residual stresses and distortions in GMA welding of thin dissimilar AA5052-AA6061 plates. *J. Manuf. Process.* **2017**, *25*, 340–350. [\[CrossRef\]](#)
29. Laksha; Bharti, P.; Khanna, P. Prediction of angular distortion in MIG welding of stainless steel 202 plates. In *Advances in Mechanical and Materials Technology: Select Proceedings of EMSME*; Springer: Singapore, 2022; pp. 525–536.
30. Lohate, M.S.; Damale, A.V. Fuzzy based prediction of angular distortion of gas metal arc welded structural steel plates. *Int. J. Innov.* **2015**, 2394–3696.
31. Baskoro, A.S.; Hidayat, R.; Widianto, A.; Amat, M.A.; Putra, D.U. Optimization of Gas Metal Arc Welding (GMAW) parameters for minimum distortion of t welded joints of A36 mild steel by Taguchi method. *Mater. Sci. Forum* **2020**, *1000*, 356–363. [\[CrossRef\]](#)
32. Xie, D.; Zhao, J.; Liang, H.; Liu, S.; Tian, Z.; Shen, L.; Wang, C. Cause of angular distortion in fusion welding: Asymmetric cross-sectional profile along thickness. *Materials* **2019**, *12*, 58. [\[CrossRef\]](#)
33. Yu, R.; Zhao, Z.; Bai, L.; Han, J. Prediction of weld reinforcement based on vision sensing in GMA additive manufacturing process. *Metals* **2020**, *10*, 1041. [\[CrossRef\]](#)
34. Cochran, W.G.; Cox, G.M. *Experimental Designs*, 2nd ed.; Wiley: Hoboken, NJ, USA, 1992.
35. Sudhakaran, R.; VeL Murugan, V.; Senthil Kumar, K.M.; Jayaram, R.; Pushparaj, A.; Praveen, C.; Venkat Prabhu, N. Effect of welding parameters on weld bead geometry and optimization of process parameters to maximize depth to width ratio for stainless steel gas tungsten arc welded plates using genetic algorithm. *Eur. J. Sci. Res.* **2011**, *62*, 76–94.
36. Shim, J.Y.; Zhang, J.W.; Yoon, H.Y.; Kang, B.Y.; Kim, I.S. Prediction model for bead reinforcement area in automatic gas metal arc welding. *Adv. Mech. Eng.* **2018**, *10*, 1687814018781492. [\[CrossRef\]](#)
37. Zain, A.M.; Haron, H.; Sharif, S. Prediction of surface roughness in the end milling machining using artificial neural network. *Expert Syst. Appl.* **2010**, *37*, 1755–1768. [\[CrossRef\]](#)

38. Narayanareddy, V.V.; Chandrasekhar, N.; Vasudevan, M.; Muthukumaran, S.; Vasantharaja, P. Numerical simulation and artificial neural network modeling for predicting welding-induced distortion in butt-welded 304L stainless steel plates. *Metall. Mater. Trans. B* **2016**, *47*, 702–713. [\[CrossRef\]](#)
39. Li, Y.; Lee, T.H.; Wang, C.; Wang, K.; Tan, C.; Banu, M.; Hu, S.J. An artificial neural network model for predicting joint performance in ultrasonic welding of composites. *Procedia CIRP* **2018**, *76*, 85–88. [\[CrossRef\]](#)
40. Jacques, L.; El Ouafi, A. ANN based predictive modeling of weld shape and dimensions in laser welding of galvanized steel in butt joint configurations. *JMMCE* **2018**, *6*, 316. [\[CrossRef\]](#)
41. Oussaid, K.; El Ouafi, A. A study on prediction of weld geometry in laser overlap welding of low carbon galvanized steel using ANN-based models. *J. Softw. Eng. Appl.* **2019**, *12*, 509. [\[CrossRef\]](#)
42. Saeed, M.M.; Al Sarraf, Z.S. Using artificial neural networks to predict the effect of input parameters on weld bead geometry for saw process. *J. Eur. Syst. Autom.* **2021**, *54*, 309–315. [\[CrossRef\]](#)
43. Jacques, L.; El Ouafi, A. Prediction of Weld joint shape and dimensions in laser welding using a 3d modeling and experimental validation. *Mater. Sci. Appl.* **2017**, *8*, 757–773. [\[CrossRef\]](#)
44. Zubairuddin, M.; Chaurasia, P.K.; Ali, B. Thermo-mechanical analysis of laser welding of Grade 91 steel plates. *Optik* **2021**, *245*, 167510. [\[CrossRef\]](#)
45. Zubairuddin, M.; Albert, S.K.; Reddy, M.S.; Ali, B.; Varaprasad, B.; Mishra, A.; Das, P.K.; Elumalai, P.V. Thermal analysis of thin P91 steel using FlexPDE and SYSWELD. *Mater. Today Proc.* **2023**, *72*, 1550–1555. [\[CrossRef\]](#)
46. Kumar, P.; Kumar, R.; Arif, A.; Veerababu, M. Investigation of numerical modelling of TIG welding of austenitic stainless steel (304L). *Mater. Today Proc.* **2020**, *27*, 1636–1640. [\[CrossRef\]](#)
47. Afzal, A.; Aabid, A.; Khan, A.; Khan, S.A.; Rajak, U.; Verma, T.N.; Kumar, R. Response Surface Analysis, Clustering, and Random Forest Regression of Pressure in Suddenly Expanded High-Speed Aerodynamic Flows. *Aerosp. Sci. Technol.* **2020**, *107*, 106318. [\[CrossRef\]](#)
48. Afzal, A.; Ansari, Z.; Faizabadi, A.R.; Ramis, M.K. Parallelization Strategies for Computational Fluid Dynamics Software: State of the Art Review. *Arch. Comput. Methods Eng.* **2017**, *24*, 337–363. [\[CrossRef\]](#)
49. Afzal, A.; Abdul Mujebe, M. Thermo-Mechanical and Structural Performances of Automobile Disc Brakes: A Review of Numerical and Experimental Studies. *Arch. Comput. Methods Eng.* **2019**, *26*, 1489–1513. [\[CrossRef\]](#)
50. Pinto, R.N.; Afzal, A.; D'Souza, L.V.; Ansari, Z.; Mohammed Samee, A. Computational Fluid Dynamics in Turbomachinery: A Review of State of the Art. *Arch. Comput. Methods Eng.* **2017**, *24*, 467–479. [\[CrossRef\]](#)
51. Jilte, R.; Afzal, A.; Panchal, S. A Novel Battery Thermal Management System Using Nano-Enhanced Phase Change Materials. *Energy* **2021**, *219*, 119564. [\[CrossRef\]](#)
52. Ağbulut, Ü.; Saridemir, S.; Rajak, U.; Polat, F.; Afzal, A.; Verma, T.N. Effects of High-Dosage Copper Oxide Nanoparticles Addition in Diesel Fuel on Engine Characteristics. *Energy* **2021**, *229*, 120611. [\[CrossRef\]](#)
53. Afzal, A.; Bhutto, J.K.; Alrobaian, A.; Kaladgi, A.R.; Khan, S.A. Modelling and Computational Experiment to Obtain Optimized Neural Network for Battery Thermal Management Data. *Energies* **2021**, *14*, 7370. [\[CrossRef\]](#)
54. Mokashi, I.; Afzal, A.; Khan, S.A.; Abdullah, N.A.; Bin Azami, M.H.; Jilte, R.D.; Samuel, O.D. Nusselt Number Analysis from a Battery Pack Cooled by Different Fluids and Multiple Back-Propagation Modelling Using Feed-Forward Networks. *Int. J. Therm. Sci.* **2021**, *161*, 106738. [\[CrossRef\]](#)
55. Chaluvvaraju, B.V.; Afzal, A.; Vinnik, D.A.; Kaladgi, A.R.; Alamri, S.; Tirth, V. Mechanical and Corrosion Studies of Friction Stir Welded Nano Al₂O₃ Reinforced Al-Mg Matrix Composites: RSM-ANN Modelling Approach. *Symmetry* **2021**, *13*, 537. [\[CrossRef\]](#)
56. Afzal, A.; Khan, S.A.; Saleel, C.A. Role of Ultrasonication Duration and Surfactant on Characteristics of ZnO and CuO Nanofluids. *Mater. Res. Express* **2019**, *6*, 1150d8. [\[CrossRef\]](#)
57. Afzal, A.; Nawfal, I.; Mahbulul, I.M.; Kumbar, S.S. An Overview on the Effect of Ultrasonication Duration on Different Properties of Nanofluids. *J. Therm. Anal. Calorim.* **2019**, *135*, 393–418. [\[CrossRef\]](#)
58. Afzal, A.; Navid, K.M.Y.; Saidur, R.; Razak, R.K.A.; Subbiah, R. Back Propagation Modeling of Shear Stress and Viscosity of Aqueous Ionic - MXene Nanofluids. *J. Therm. Anal. Calorim.* **2021**, *145*, 2129–2149. [\[CrossRef\]](#)
59. Bakır, H.; Ağbulut, Ü.; Gürel, A.E.; Yıldız, G.; Güvenç, U.; Soudagar, M.E.M.; Hoang, A.T.; Deepanraj, B.; Saini, G.; Afzal, A. Forecasting of Future Greenhouse Gas Emission Trajectory for India Using Energy and Economic Indexes with Various Metaheuristic Algorithms. *J. Clean. Prod.* **2022**, *360*, 131946. [\[CrossRef\]](#)
60. David, O.; Waheed, M.A.; Taheri-Garavand, A.; Nath, T.; Dairo, O.U.; Bolaji, B.O.; Afzal, A. Prandtl Number of Optimum Biodiesel from Food Industrial Waste Oil and Diesel Fuel Blend for Diesel Engine. *Fuel* **2021**, *285*, 119049. [\[CrossRef\]](#)
61. David, O.; Okwu, M.O.; Oyejide, O.J.; Taghinezhad, E.; Asif, A.; Kaveh, M. Optimizing Biodiesel Production from Abundant Waste Oils through Empirical Method and Grey Wolf Optimizer. *Fuel* **2020**, *281*, 118701. [\[CrossRef\]](#)
62. Sharath, B.N.; Venkatesh, C.V.; Afzal, A. Multi Ceramic Particles Inclusion in the Aluminium Matrix and Wear Characterization through Experimental and Response Surface-Artificial Neural Networks. *Materials* **2021**, *14*, 2895. [\[CrossRef\]](#)
63. Afzal, A.; Saleel, C.A.; Badruddin, I.A.; Khan, T.M.Y.; Kamangar, S.; Mallick, Z.; Samuel, O.D.; Soudagar, M.E.M. Human Thermal Comfort in Passenger Vehicles Using an Organic Phase Change Material—An Experimental Investigation, Neural Network Modelling, and Optimization. *Build. Environ.* **2020**, *180*, 107012. [\[CrossRef\]](#)

64. Afzal, A.; Mokashi, I.; Khan, S.A.; Abdullah, N.A.; Azami, M.H.B. Optimization and Analysis of Maximum Temperature in a Battery Pack Affected by Low to High Prandtl Number Coolants Using Response Surface Methodology and Particle Swarm Optimization Algorithm. *Numer. Heat Transf. Part A Appl.* **2020**, *79*, 406–435. [[CrossRef](#)]
65. Afzal, A.; Khan, S.A.; Islam, T.; Jilte, R.D.; Khan, A.; Soudagar, M.E.M. Investigation and Back-Propagation Modeling of Base Pressure at Sonic and Supersonic Mach Numbers. *Phys. Fluids* **2020**, *32*, 096109. [[CrossRef](#)]
66. Sathish, T.; Kaladgi, A.R.R.; Mohanavel, V.; Arul, K.; Afzal, A.; Aabid, A. Experimental Investigation of the Friction Stir Weldability of AA8006 with Zirconia Particle Reinforcement and Optimized Process Parameters. *Materials* **2021**, *14*, 2782. [[CrossRef](#)] [[PubMed](#)]
67. Afzal, A.; Samee, A.D.M.; Javad, A.; Shafvan, S.A.; Ajinas, P.V.; Kabeer, K.M.A. Heat Transfer Analysis of Plain and Dimpled Tubes with Different Spacings. *Heat Transf. Res.* **2018**, *47*, 556–568. [[CrossRef](#)]

Disclaimer/Publisher's Note: The statements, opinions and data contained in all publications are solely those of the individual author(s) and contributor(s) and not of MDPI and/or the editor(s). MDPI and/or the editor(s) disclaim responsibility for any injury to people or property resulting from any ideas, methods, instructions or products referred to in the content.